**SANDIA REPORT**

SAND99–0746
Unlimited Release
Printed April 1999



# Ultra-Precise Assembly of Micro-Electromechanical Systems (MEMS) Components

John T. Feddema, Ron Simon, Marc Polosky, Todd Christenson

Prepared by
Sandia National Laboratories
Albuquerque, New Mexico 87185 and Livermore, California 94550

Sandia is a multiprogram laboratory operated by Sandia Corporation, a Lockheed Martin Company, for the United States Department of Energy under Contract DE-AC04-94AL85000.



Sandia National Laboratories

Issued by Sandia National Laboratories, operated for the United States Department of Energy by Sandia Corporation.



Available to DOE and DOE contractors from
Office of Scientific and Technical Information
P.O. Box 62
Oak Ridge, TN 37831

Prices available from (615) 576-8401, FTS 626-8401

Available to the public from
National Technical Information Service
U.S. Department of Commerce
5285 Port Royal Rd
Springfield, VA 22161

NTIS price codes
Printed copy: A11
Microfiche copy: A01

SAND99-0746
Unlimited Release
Printed April 1999

# Ultra-Precise Assembly of Micro-Electromechanical Systems (MEMS) Components

John T. Feddema
Intelligent Systems, Sensors & Controls Department

Ronald W. Simon
Intelligent Systems Principles Department

Marc A. Polosky
Electromechanical Engineering Department

Todd R. Christenson
Advanced Semiconductor Technology Department

Sandia National Laboratories
P.O. Box 5800
Albuquerque, NM 87185-1003

## Abstract

This report summarizes a three year effort to develop an automated microassembly workcell for the assembly of LIGA (Lithography Galvonoforming Abforming) parts. Over the last several years, Sandia has developed processes for producing surface machined silicon and LIGA parts for use in weapons surety devices. Some of these parts have outside dimensions as small as 100 micron, and most all have submicron tolerances. Parts this small and precise are extremely difficult to assembly by hand. Therefore, in this project, we investigated the technologies required to develop a robotic workcell to assembly these parts. In particular, we concentrated on micro-grippers, visual servoing, micro-assembly planning, and parallel assembly. Three different micro-grippers were tested: a pneumatic probe, a thermally actuated polysilicon tweezer, and a LIGA fabricated tweezer. Visual servoing was used to accuracy position two parts relative to one another. Fourier optics methods were used to generate synthetic microscope images from CAD

drawings. These synthetic images are used off-line to test image processing routines under varying magnifications and depths of field. They also provide reference image features which are used to visually servo the part to the desired position. We also investigated a new aspect of fine motion planning for the micro-domain. As parts approach 1-10 μm or less in outside dimensions, interactive forces such as van der Waals and electrostatic forces become major factors which greatly change the assembly sequence and path plans. We developed the mathematics required to determine the goal regions for pick up, holding, and release of a micro-sphere being handled by a rectangular tool. Finally, we implemented and tested the ability to assemble an array of LIGA parts attached to two 3 inch diameter wafers. In this way, hundreds of parts can be assembled in parallel rather than assembling each part individually.

**Acknowledgements**

Many Sandians and non-Sandians contributed to this project. The authors thank Barry Spletzer for designing the vacuum probe, David Armor for designing the pin insertion tool, Merlin Decker for designing the pin holder and press-fit wafer, and Andy Jojola for chamfering the pins. We also thank Patrick Xavier and Russell Brown for their input on assembly planning. Finally, we thank Chris Keller of MEMS Precision Instruments for the use of his polysilicon tweezers, and Jim Barr from Vanderbilt University for programming the robot for the parallel assembly tests.

This page intentionally left blank.

# Contents

# Figures

# Tables

## 1.0 Introduction

In recent years, the world economy has seen expansive market growth in the area of MEMS (Micro-ElectroMechanical Systems). It is predicted that the MEMS market could reach more than $34 billion by the year 2002. Today, commercially available MEMS products include accelerometers for airbags and inkjet printer heads. These products require little or no assembly because a monolithic integrated circuit process is used to develop the devices. However, future MEMS products may not be as fortunate. Monolithic integration is not feasible when incompatible processes, complex geometry, or different materials are involved. For these cases, new and extremely precise micro-manipulation capabilities will be required for successful product realization.

Sandia National Laboratories is currently developing manufacturing processes to make MEMS parts with 10-100 micron outer dimensions and submicron tolerance for use in weapons surety devices. In particular, Sandia is pursuing both surface machined silicon and LIGA (Lithography Galvonoforming Abforming) parts. The surface machined silicon devices are fabricated in place using several layers of etched silicon and generally do not require assembly. However, the LIGA parts are batch fabricated and do require assembly. The LIGA parts are formed by using X-ray lithography to create molds in PMMA (polymethylmethacrylate) and then electroplating metals (typically nickel, permalloy, and copper) in the molds. Afterwards, the metal parts are released into Petrie dishes. LIGA parts are of special interest because they can be made thicker than silicon parts (hundreds of microns verses tens of microns), and they can be made of metals which makes them stronger in tension than surface machined silicon. The disadvantage of LIGA parts over silicon structures is that they must be assembled. The required precision, operator stress and eye strain associated with assembling such minute parts under a microscope generally precludes manual assembly from being a viable option. An automated assembly system addresses these problems.

There are several issues that cause micro-assembly to be a difficult assembly problem. As discussed in [1][2], the relative importance of the forces in microassembly is very different from that in the macro world. Gravity is almost negligible, while surface adhesion and electrostatic forces dominate. To some extent, these problems can be reduced by cleaning parts and electrically grounding surfaces. However, the effects of these forces are still visible during even the simplest of tasks.

To date, several different approaches to teleoperated micromanipulation have been attempted. Miyazaki [3] and Kayono [4] meticulously picked up 35 polymer particles (each 2 microns in diameter) and stacked them inside of a scanning electron microscope (SEM). Controlling the contact surface of a gold plated needle allowed them to pick up and release the particles. Mitsuishi [5] developed a teleoperated, force-reflecting, micromachining system under a SEM. Sulzmann [7] teleoperated a microrobot using 3D computer graphics (virtual reality) as the user interface.

Even with these efforts, grasping and releasing micron sized parts continues to be a largely unsolved problem. For some tasks, vacuum grippers appear to be adequate. Zesch [7] used a vacuum gripper to pick up 100 micron size diamond crystals and deposit them to arbitrary locations. However, for other tasks involving metallic parts with irregular shapes, more dexterous microtweezers are needed. Keller [8] developed a high aspect ratio molded polysilicon (hexsil) tweezers. These tweezers are actuated by in-situ phosphorous doped thermal expansion beams. Piezoresistive polysilicon strain gages are integrated into the tweezers for tactile feedback. Ballandras [9] developed LIGA fabricated micro-grippers. These tweezers where actuated with a PZT (piezoelectric transducer).

In this report, we describe our efforts over the last three years to develop a fully automated microassembly workcell. Much of the material in this report can also be found in conference and journal publications [10-16]. The next section describes the microassembly workcell used in the experiments. This is followed by sections on micro-grippers, CAD-driven visual servoing, microassembly planning, and parallel assembly of LIGA.

## 2.0 Microassembly Workcell

Our microassembly workcell consists of a 4 DOF (Degree of Freedom) AMTI (subsidiary of ESEC) Cartesian assembly system, a 4 DOF precision stage, micro-tweezers, and a long working distance microscope (see Figure 2.1 and 2.2). The AMTI robot has a repeatability of 0.4 microns in the *x* and *y* directions, 8 microns in the *z* direction, and 23.56 arc-seconds in rotation about *z*. The precision stage has a repeatability of approximately 1 micron in *x, y,* and *z*, and 1.8 arc-seconds in rotation about *z*. The microscope is fixed above the stage and has an electronically adjustable zoom and focus.

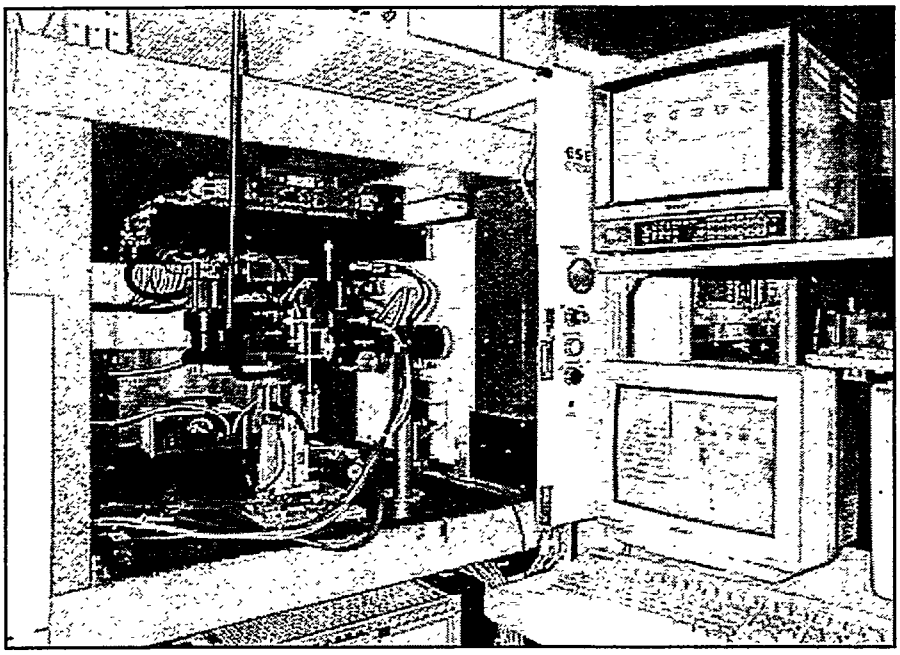

*Figure 2.1. Micro-assembly workcell.*

During assembly operations, the AMTI robot positions the micro-tweezers above the stage and within the field of view of the microscope. The precision stage is used to move the LIGA parts between the fingers of the tweezers. The tweezers are closed on the part, the stage is lowered, and the mating part on the stage is brought into the field of view. The stage is then raised into position and the part in the tweezers is released.

A teleoperated interface was developed to test simple pick-and-place operations. The AMTI robot, the 4 DOF precision stage, the micro-tweezers, and the focus, magnification, and lighting of the microscope are controlled through a custom developed user interface built within the Adept A-series VME controller. The image of the parts as seen by the microscope is displayed on the computer screen. The *x* and *y* position of the robot and stage are controlled by the operator

by dragging a cursor on the graphical display. Sliders are used to control the *z* position and theta orientation of the robot and stage as well as the microscope focus, magnification, and lighting.

This teleoperated interface has been used to pick up and place 100 micron O.D. LIGA gears with a 50 micron hole on pins ranging from 35 to 44 microns (see Figure 2.3). The next section describes the micro-grippers used to handle the parts.

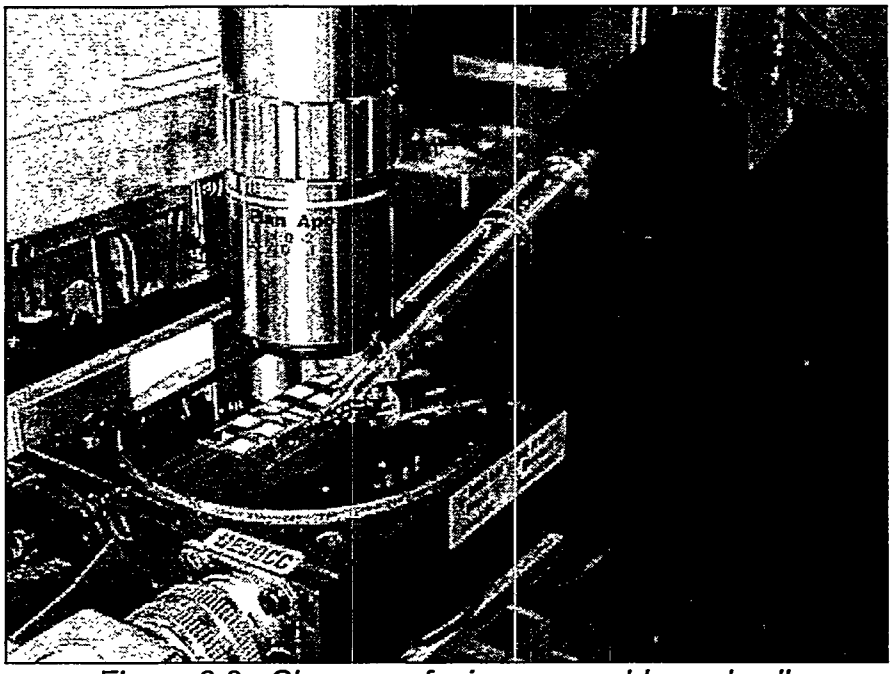

*Figure 2.2. Close up of micro-assembly workcell.*

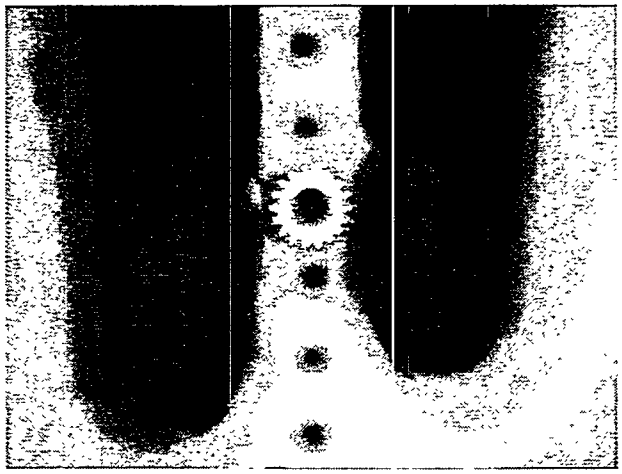

*Figure 2.3. LIGA tweezers placing LIGA gear on a 44 micron OD shaft.*

## 3.0 Micro-grippers

Three grasping techniques were evaluated for placing the 100 micron OD LIGA gears with 50 micron inner diameter (ID) holes on LIGA posts with diameters ranging from 35 microns to 49 microns. The first technique uses a simple vacuum gripper with a pair of three-way valves which provide negative pressure to pick up the part and positive pressure to release the part. The second grasping technique is a thermally actuated Hexsil polysilicon tweezers from University of California, Berkeley. The third grasping technique is a LIGA fabricated tweezers which is actuated by a linear ball-and-screw DC motor and a collet style closing mechanism. These three techniques are discussed in the following three sections.

### 3.1 Vacuum Gripper

The vacuum gripper used in our tests is a 304 stainless steel tube, approximately 10 mm long and 100 microns in outside diameter. It is press fit into a brass housing. Air flow to create vacuum and force are supplied through the housing by an air line connected to the rear of the housing and a hole through the housing. The strength of the flow is controlled by a needle valve inline with the air line. The vacuum gripper exits the housing at an angle of approximately 30 degrees. This allows use of the vision system to monitor the location of the tip, and operations taking place when the parts are picked up or dropped.

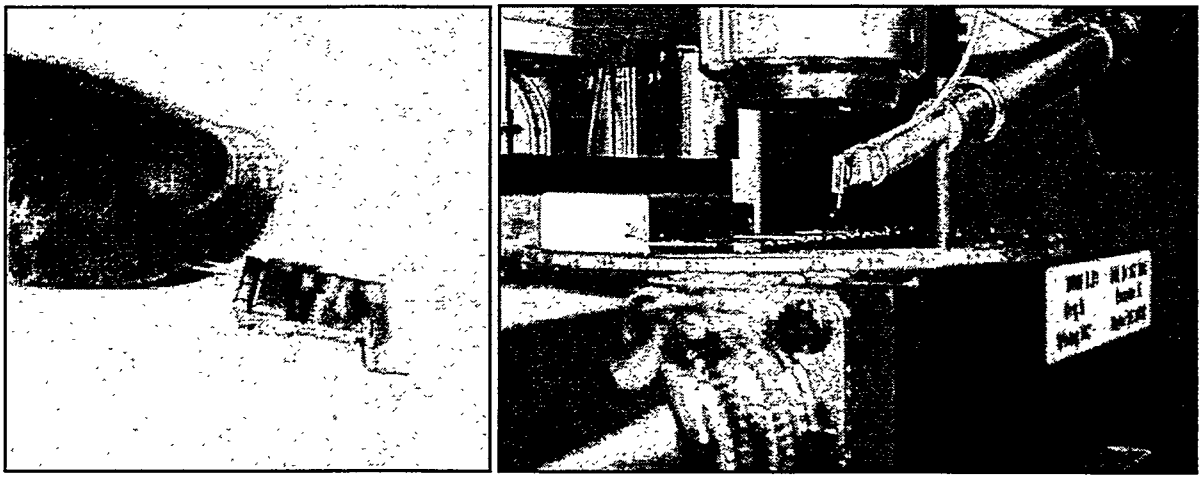

*Figure 3.1. Vacuum gripper.*

Initial testing demonstrated high reliability in acquisition of the parts (permalloy gears with 50 micron ID, and 100 micron OD). Releasing of the parts was more difficult. In the absence of physical constraints in the drop location, the quantity of

flow required to blow the part off the tip guaranteed the part would be blown far from the desired drop point. This did not seem consistent with the ease with which the part was acquired, using very little vacuum pressure to pick it up.

To test the possibility that other forces were responsible for part acquisition, the vacuum was turned off during part acquisition. The vacuum gripper was positioned above the part. Incremental (10 micron steps) approaches to the part were used to determine if acquisition was possible through contact forces when the gripper touched the part. Part acquisition occurred approximately 50 microns above the part. This test was repeated several times with the same result. Further investigation showed the vacuum gripper was magnetic.

Although 304 stainless is supposed to be non-magnetic, it appears a permanent magnetic field was introduced onto the tubing when it was manufactured, possibly when cold drawn. We have begun to search for non-magnetic materials to be used as tubing, concentrating at this point on glass. The required size of the tubing is a severe constraint, but we believe it can be found in the medical community.

### 3.2 Hexsil Tweezers

High aspect ratio molded polysilicon (hexsil) [17] tweezers from the Berkeley Sensor & Actuator Center were mounted on the AdeptOne tool plate. These tweezers are actuated by in-situ phosphorous doped thermal expansion beams. Piezoresistive polysilicon strain gages are integrated into the tweezers for tactile feedback. The tweezers are normally closed, and require 75 mW to open 35 microns. The piezoresistive strain gages are not yet operational, but, as described later, will greatly enhance operation in the future.

Figure 3.2 shows the 8 mm long by 1.5 mm wide by 45 micron thick hexsil tweezers in the open (power on) position. The thermal expansion element is electrically isolated from the rest of the device. Current travels up one leg and down the other. The beam heats up and lengthens, causing the other beams in the two 4-bar linkages to rotate and open the tweezers tips. Thermal actuation has the advantages of simple fabrication and reliability with no sliding contacts which would be vulnerable to failure due to wear or contamination. The beam was made relatively long (6mm) to minimize the operating temperature for a given displacement.

High out-of-plane stiffness is desirable to ensure the tweezers tips will contact each other when the tweezers are closed. Any z-axis mismatch between the tips would apply a torque to the object being gripped, causing it to flip out of the grip. The hexsil fabrication process conveniently supplies the needed out-of-plane stiffness. On the other hand, in-plane stiffness should be low for efficient actuation, and sub-micro-Newtons resolution of the gripping force being applied to a fragile object. Hexsil fabrication provides flexures for linkages with low in-plane stiffness. Surface poly tweezer tips built on the hexsil foundation give the compliance for the required force resolution at the target object. Progressively larger beams make the transition from the micro to macro stiffnesses. In use, the base of the tweezer is

bonded to a 2 mm wide, 25 mm long silicon bar that mounts into a fixture on the AdeptOne tool plate. In the absence of the piezoresistors, observation by optical microscope of the tweezers tip deflection indicates the gripping force. The maximum design stress in the hexsil flexures is compressive and less than 1 MPa, while the thermal expansion beam is maintained under a tensile stress of less than 0.1 MPa.

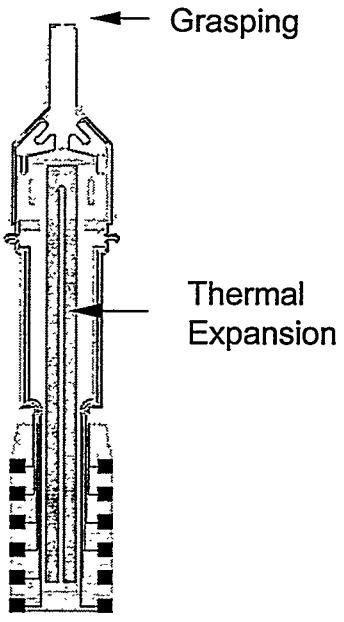


*Figure 3.2. Hexsil tweezers.*

This teleoperated interface has been used to pick up and stack two LIGA gears and up to 5 polysilicon gears (see Figure 3.3). The key issues discovered while performing these operations are as follows.

1. Currently, the only way to estimate when the micro-tweezers have a good grasp of the part is by watching the deflections in the tweezers. The future incorporation of the tweezer's strain gages will greatly improve the ability to detect when a good grasp has been achieved.

2. When grasping a part, it is not always possible to tell if the tweezers are at the same height as the part. We often had to touch the tweezers to the part to see if it moved.

3. When stacking parts, the part on the stage was lowered and moved in x-y directions while the part in the tweezers stayed fixed. The result is that the part in the tweezers remains in focus while the part on the stage was out of focus. Even with the bottom part out-of-focus, the human operator is able to line up

important image features; however, it is still very difficult to estimate height above the bottom part.

4. Since the LIGA gears were made out of permalloy (a magnetic material), we had problems with the parts being attracted to each other.

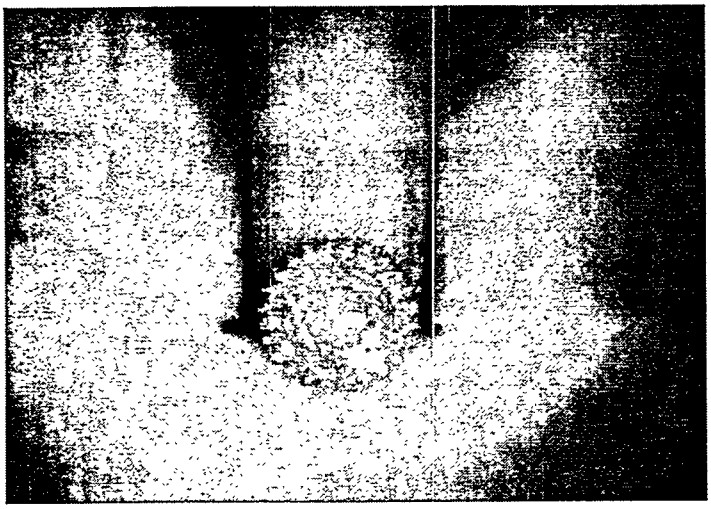

*Figure 3.3. Hexsil micro-tweezers picking up LIGA gear.*

### 3.3 LIGA Fabricated Tweezers

The third grasping technique utilizes LIGA fabricated tweezers, a linear ball-and-screw DC motor, and a collet style closing mechanism (see Figure 3.4). For those unfamiliar with a collet, a brief description is provided. A collet is a holding fixture normally used in a lathe to constrain raw stock for machining. It is best described as a tube split longitudinally along two thirds its length into three equal sections. The end of the tube that is split has an external taper while the other end is treaded externally. A sleeve with an internal taper is fitted over the treaded end of the tube and engages the tapered split ends. As the sleeve is advanced, the three equally-spaced split sections move radially inward thus providing a clamping mechanism for material positioned inside the tube.

The tube used in the collet mechanism has two split ends versus three. As the sleeve is advanced forward, the split halves move directly toward each other, similar to a closing pair of tweezers. As the sleeve is advanced in the reverse direction, the split halves reopen (see Figure 3.5). Machined into the tips of the spit halves are features used to constrain a smaller pair of tweezers fabricated using the LIGA process. The LIGA process enables the fabrication of a large number of tweezer variations (with submicron tolerances) at a moderate price. Many variations of LIGA tweezers can be interchangeably used with this collet mechanism. Thus the tweezers can be fabricated for easy manipulation of parts

with unique profiles. Parts ranging in size from several millimeters to tens of microns can be handled (this part size range was a requirement for the design of the tweezers).

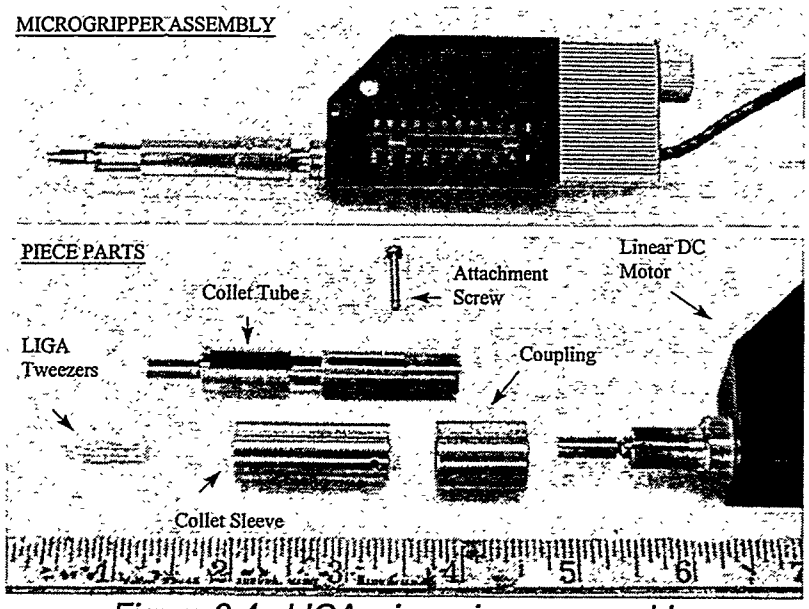


*Figure 3.4. LIGA microgripper assembly.*

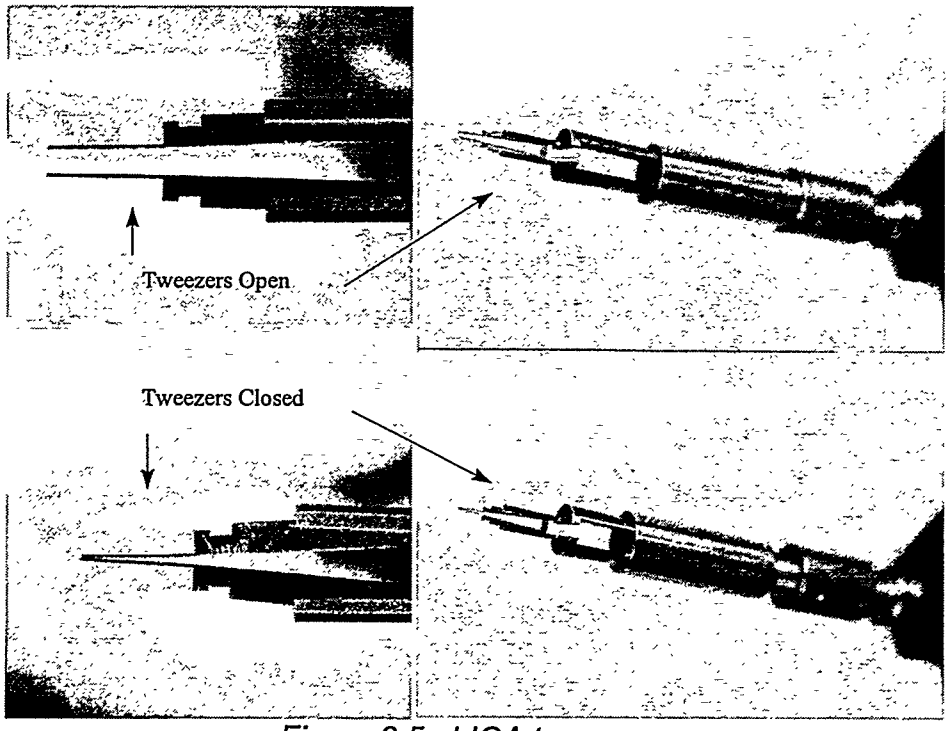


*Figure 3.5. LIGA tweezers.*

A Newport 850F HS linear DC motor is used to hold the collet tube and drive the collet sleeve. The encoder resolution is 0.59 microns. Maximum speed is 4.75 mm/sec, and maximum axial load is 22.54 N. Backlash is listed as less than 15 microns and bidirectional repeatability is better than one micron when backlash is compensated by the controller. For a 1.5 degree collet taper, a value for the resolution in the gripping direction is calculated to be 0.025 microns (see Figure 3.6 and Equation (3.1) below).

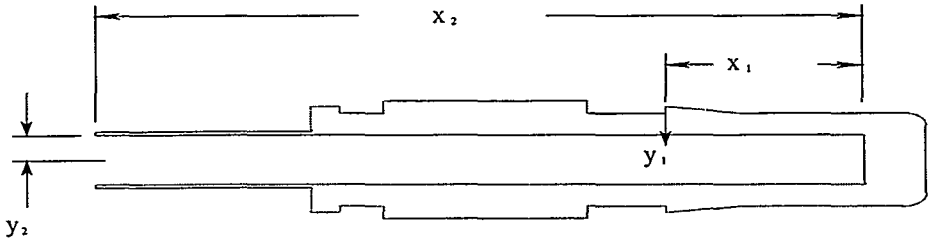


*Figure 3.6. LIGA tweezer resolution.*

$$y_2 = \frac{x_2}{x_1} y_1 \tag{3.1}$$

where: $x_1$ = 13.1 mm
$x_2$ = 21.1 mm
$y_1$ = $\Delta X \tan(\theta)$ (Displacement of Collet)
$\Delta X$ = 0.59 μm (DC Motor Resolution)
$\theta$ = 1.5 deg. (Collet Tube Taper)
$y_2$ = 0.025 μm (Resolution in the Gripping Direction)

Three materials have been used to fabricate the LIGA tweezers: copper, nickel, and Permalloy 78/22 (78%Nickel, 22% Iron). Permalloy possesses the best mechanical properties and functions best mechanically; while copper is nonmagnetic and eliminates adverse effects due to residual magnetism inherent in Permalloy and nickel parts.

When designing the the LIGA tweezers, we took special care to make sure that the tweezers did not plastically deform when they were closed. Using Figure 3.7, the deflection of the tip is given by

$$y = \frac{-F}{6EI}\left(2L^3 - 3L^2 a + a^3\right) \tag{3.2}$$

where $F$ is the force exerted by the collet, $E$ is the Young's modulus of the material, $I$ is the moment of inertia, $L$ is the length of the tweezer with respect to the

base, and $a$ is the length of the tweezer with respect to where it is closed by the collet.

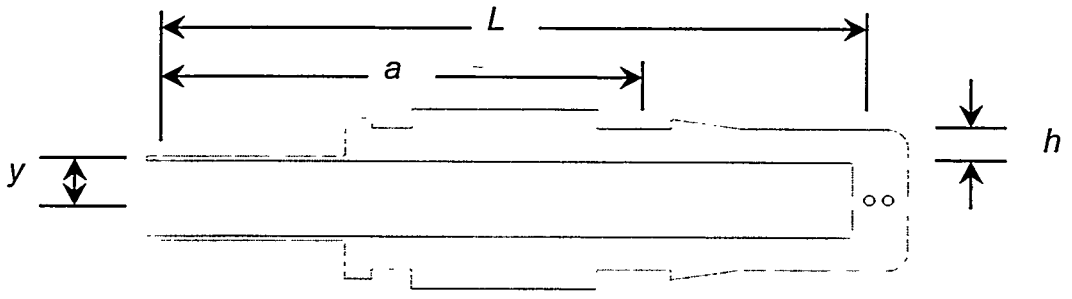


*Figure 3.7. Notation used for stress calculations.*

The stress at the base of the micro-gripper is given by

$$\sigma = \frac{F(L-a)(h/2)}{I} \tag{3.3}$$

where $h$ is the thickness of the tweezers at the base. Combining Equations (3.2) and (3.3), the stress at the base of the micro-gripper is

$$\sigma = \frac{-3Eh(L-a)y}{\left(2L^3 - 3L^2a + a^3\right)} \tag{3.4}$$

Table 3.1 shows example calculated dimensions for Permalloy, nickel, and copper. The safety factor is the ratio of the calculated stress for the given dimensions over the yield stress of the material. Notice how the copper micro-gripper had to be made much longer than the Permalloy or nickel micro-grippers because of copper's larger Young's modulus.

*Table 3.1. Examples of stress calculations.*

| Material | L (m) | a (m) | y (m) | E (N/m$^2$) | h (m) | σ (m) | Safety Factor |
|---|---|---|---|---|---|---|---|
| Ni78Fe22 | 2.11e-2 | 1.32e-2 | 1.27e-2 | 8.62e+10 | 6.00e-4 | 4.47e+8 | 2.93 |
| Nickel | 2.11e-2 | 1.32e-2 | 1.27e-2 | 5.52e+10 | 6.00e-4 | 2.86e+8 | 1.92 |
| Copper | 2.11e-2 | 1.32e-2 | 1.27e-2 | 1.17e+11 | 6.00e-4 | 6.08e+8 | 0.14 |
| Copper | 4.41e-2 | 1.23e-2 | 1.27e-2 | 1.17e+11 | 6.00e-4 | 8.37e+7 | 1.01 |

To accommodate interchanging tweezers, a tweezer tool holder has been designed (see Figure 3.8). The holder will accommodate six different tweezer designs and enable the tweezers to be loaded robotically. The tweezers are first driven closed, inserted into the tool holder, and then driven to the halfway open position. A notch on the front end of the tweezer is captured in a slot located inside the tool holder. The collet mechanism is then driven to the fully open position, which releases the tweezers, and withdrawn from the tool holder. To load a new pair of tweezers, the process is repeated in the reverse order.

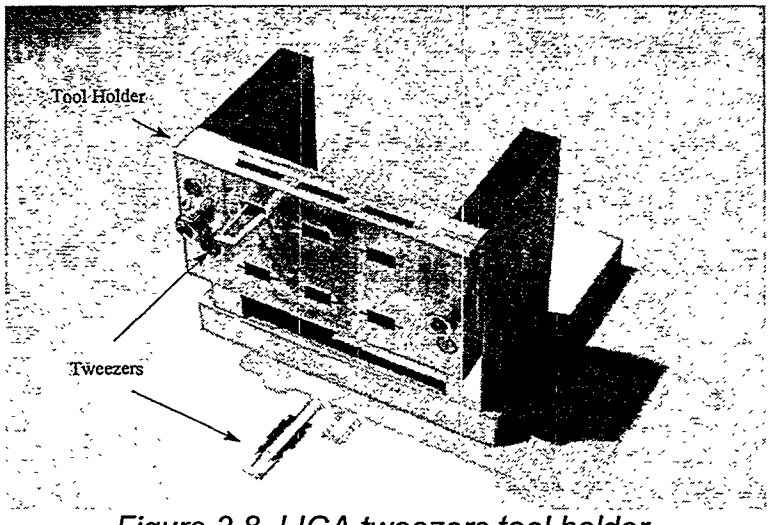


*Figure 3.8. LIGA tweezers tool holder.*

In experimental tests, we have demonstrated the ability to pick up and stack LIGA and polysilicon gears using these tweezers. Initially, human or machine vision were the only methods of detecting when the gear is inside the tweezers. Since there was no force feedback, it was very difficult to estimate how good of a grasp was being made. Micro-strain gauges were added to the tweezers' fingers to eventually detect when a part is grasped and to help guide the gear onto the post.

Thin film silicon strain gauges were fabricated onto each finger of the LIGA tweezers. The physical size of the strain gauges required that the width of the surface, where the strain gauges were mounted, be at least 200 microns. Because of this restriction, we had to settle with mounting the strain gauges on the top and bottom of each tweezer finger approximately 6 mm from the ends of the finger tips. While this precludes force sensing in the directions required for grip detection, it does provide sensing which can be used when approaching the working surface in a guarded move. Thirty-eight gauge single stranded wire is jumpered from the strain gauges to pads on the fingers of the tweezers. The bridge is completed, balanced and temperature compensated using a small PC board and a 22 cm

pigtail from the pads. Power (5Vdc) and ground is applied to the PC board, and the bridge output is fed to an input A/D amplifier for sampling and detection. Software was written to poll the A/D output and provide certain types of motion interrupts as required.

The force sensor was tested by positioning the tweezers slightly above the surface of a glass slide holding several of the desired parts. The gripper was incrementally lowered to the glass surface, while readings were taken from the force sensor at each location. Figure 3.9 shows the force measured as a function of position. The tweezers act as a cantilevered beam as they are pushed against the glass surface.

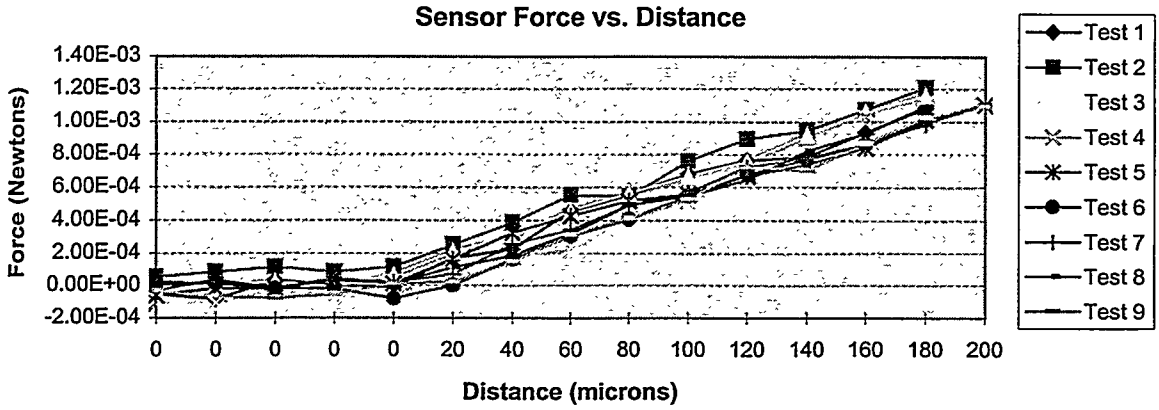


*Figure 3.9. Measured force vs. distance.*

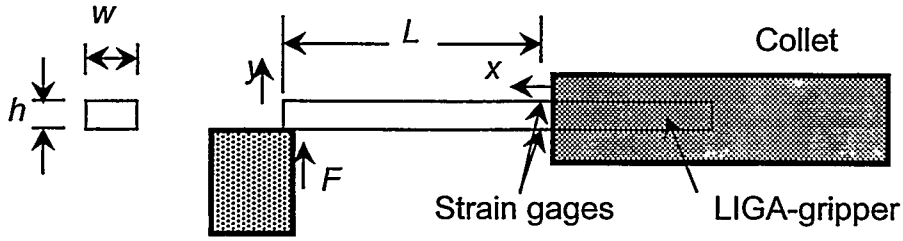


*Figure 3.10. Analysis of strain gage tests.*

The calculations used to generate Figure 3.9 where determined by analyzing Figure 3.10. The deflection at the tip of the gripper is

$$y = \frac{FL^3}{3EI_z} \tag{3.5}$$

where moment of inertia is $I_z = \frac{h^3 w}{12}$ , $F$ is the force exerted on the tip, $L$ is the length of the beam, $E$ is Young's modulus, $h$ is the beam height, and $w$ is the beam width. In the linear operating region of the material, Young's modulus is the longitudinal stress divided by the longitudinal strain or

$$E = \frac{longitudinal\,stress}{longitudinal\,strain} = \frac{\sigma_x}{\varepsilon_x} = \frac{FL\left(h/2\right)}{I_z \varepsilon_x} \tag{3.6}$$

Combining Equations (3.5) and (3.6) and assuming that the strain gage voltage is proportional to axial strain ( $\varepsilon_x = K\Delta V$ ), the force can be computed as

$$F = \frac{Eh^2 wK}{6L}\Delta V \tag{3.7}$$

where $\Delta V$ is the strain gage voltage amd the constant $K$ is determined by the off-line calibration equation

$$K = \frac{3h}{2L^2}\frac{y}{\Delta V} \; . \tag{3.8}$$

Figure 3.9 shows that the response of the strain gage was 215.5 μN/mV. Using a 12 bit A/D with a range of 0-5 Volts, the resolution of the system is 263.1 μN per A/D count. To put this in perspective, the weight of a single 100 μm O.D. LIGA gear is 0.0345 μN. Therefore, the strain gage signal would have to be amplified almost 4 orders of magnitude to detect when a gear is picked up. While this may be possible to achieve with custom electronics, we did not have the time or money to pursue this further. We suggest that future work be directed towards embedding micro-strain gages directly into the tweezers, such as Berkeley plans to do with their polysilicon tweezers.

## 4.0 CAD-Driven Visual Servoing

Over the past decade, considerable research has been performed on Robotic Visual Servoing (RVS) (see [18][19] for review and tutorial). Using real-time visual feedback, researchers have demonstrated that robotic systems can pick up moving parts, insert bolts, apply sealant, and guide vehicles. With the rapid improvements being made in computing, image processing hardware, and CCD cameras, the application of RVS techniques are now becoming widespread.

Ideal applications for RVS are typically those which require extreme precision and can not be performed cost effectively with fixturing. As the manufacturing lot size of the product increases, it is usually more cost effective to design a set of fixtures to hold the parts in the proper orientations. However, for small lot sizes and large numbers of diverse parts, vision becomes an essential sensor. Historically, computer vision has been used in a look-and-move mode where the vision system first locates the part in robot world coordinates, and then the robot moves "blindly" to that location and picks up the part. In the 1980s, computing and image processing hardware improved to the point where vision can now be used as a continual feedback sensor for controlling the relative position between the robot and the part. RVS is inherently more precise than look-and-move vision because an error-driven control law improves the relative positioning accuracy even in the presence of modeling (robot, camera, or object) uncertainties.

One ideal application for RVS which meets these requirements is the microassembly of MEMS (Micro-ElectroMechanical Systems) components. There are several reasons why RVS is ideally suited for the assembly of LIGA parts. First, from a physiological stand point, human beings exclusively use their vision sense to assemble parts this size. People do not use force feedback because they can not feel micro-Newtons of force. Second, since the LIGA parts are randomly placed in dishes and it is difficult to design parts feeders and fixturing with submicron tolerances, vision is required to locate the parts. Third, the environment under a microscope is structured and the parts are well known. Fourth, most assembly operations are 4 degrees of freedom (DOF) *(x, y, z,* and rotation about *z)* problems. These last two points greatly simplify the image processing required to recognize and locate the parts.

In addition to the above points, this problem is well suited to be a completely automated manufacturing process based on CAD information. The LIGA parts are originally designed using CAD packages such as AutoCAD, ProE, or Velum. The designs are then translated to GDSII, which is the format that the mask shops use to develop the X-ray masks for the LIGA process. Therefore, we already have CAD information on each part. Also, since X-rays are used to develop the LIGA molds, both the horizontal and vertical tolerances of the parts are quite precise (submicron horizontal tolerances, and 0.1 micron taper over 100 microns of thickness). Therefore, there is excellent correspondence between the CAD model and the actual part.

If a synthetic microscope image of the part could be created, it would solve one very important RVS issue: where do the image reference features come from? The reference features could be learned through teach-by-showing, however, this is not cost effective in an agile manufacturing environment. Instead, it would be best if the reference image features could be derived directly from the CAD model. In this way, the model could be used for assembly planning even before the parts are produced.

To date, several different approaches to teleoperated micromanipulation have been attempted. More recently, researchers have gone beyond teleoperation to using visual feedback to automatically guide micro-robotic systems. Sulzmann [20] illuminated gallium phosphate patches on a micro-gripper with an ion beam, and he used the illuminated features to locate and position the micro-gripper. Vikramaditya [21] investigated using visual servoing and depth-from-defocus to bring parts into focus and to a specified position in the image plane. The estimation of depth from focus has also been addressed by several other researchers (e.g. [22-25]).

In this section, we take the next step by creating synthetic images from CAD data. These images are used to test image processing algorithms off-line and to create reference image features which are used on-line for visual servoing. The next three subsections describe an optics model used to generate synthetic images, resolved rate visual servoing equations, as well as the CAD-Driven assembly planning work.

### 4.1 Optics Modeling

When viewing parts on the order of 100 microns in dimension, it is important to have a precise model of the optics, including models of the field of view and depth of field. This model is even more important if the assembly is to be performed automatically from CAD information. What is needed is a way to create a synthetic image before the part is even produced. Then we can design for assembly and determine off-line the required image processing routines for assembly. In this regard, Fourier optics methods can be used to create synthetic images from the CAD drawings.

First, we provide a simple review of microscope optics. In our experiments, we are using a long working distance microscope by Navitar. This microscope uses an infinity-focused objective lens. Referring to Figure 4.1, the rays emanating from a given objective point are parallel between the objective and the tube lens. The tube lens is used to focus the parallel rays onto the image plane. The magnification is calculated by dividing a focal length of the tube lens by the focal length of the objective lens [26].

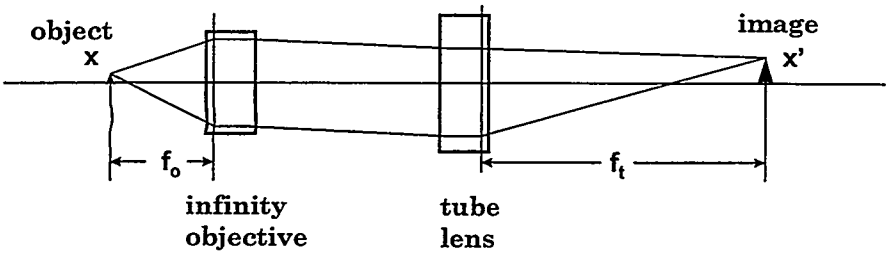


*Figure 4.1. Infinity corrected microscope optics.*

$$x' = mx \quad \text{and} \quad y' = my \qquad \text{where} \qquad m = \frac{f_t}{f_o}, \tag{4.1}$$

$(x, y)$ is the object position in the objective focal plane, $(x', y')$ is the projected position in the image plane, $m$ is the lateral magnification, $f_t$ is the focal length of the tube lens, and $f_o$ is the focal length of the objective. With our microscope, the focal length of the tube lens is adjustable so that the magnification varies from 6.9 to 44.5.

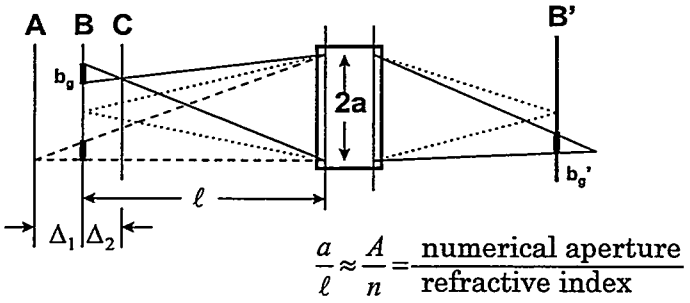


*Figure 4.2. Geometric depth of field.*

The depth of field can be determined by analyzing Figure 4.2. Here, the objective and tube lens are modeled as a single thick lens with magnification *m*. The in-focus object plane is denoted as **B**, and the corresponding in-focus image plane is denoted as **B'**. When the object is moved out of focus to planes **A** or **C**, a point on **A** or **C** is projected into a disk of diameter $b_g$ on object plane **B**. The resulting disk in the image plane has diameter $b_g'$. By using similar triangles, the geometric depth of field is given by

$$\Delta_g = \Delta_1 + \Delta_2 \approx \frac{nb_g'}{mA} \tag{4.2}$$

where *n* is the refractive index of the optics, and *A* is the numerical aperture of the optics [27]. This expression is valid if object blur $b_g$ on plane *B* is much less than the lens aperture radius *a*. Solving this equation for the defocused blur in the image,

$$b_g' = \frac{2mA|\Delta|}{n} \qquad (4.3)$$

where $\Delta = \Delta_1 \approx \Delta_2$ .

In addition to the geometric depth of field, Fraunhofer diffraction is also important as the objects being viewed approach the wavelength of light. Rayleigh's Criteria [28] says that the diameter of the Airy disk in the image plane is

$$b_r' = \frac{1.22\lambda m}{A} \qquad (4.4)$$

where $\lambda$ is the wavelength of incident light. This is the diameter of the first zero crossing in an intensity image of a point source when viewed through an ideal circular lens with numerical aperture *A* and magnification *m*.

Assuming linear optics, the geometric blur diameter and the Airy disk diameter are additive. Adding Equations (4.3) and (4.4) and solving for $\Delta$, the total depth of field is given by:

$$\Delta_T = 2\Delta = \frac{nb'}{mA} - \frac{1.22\lambda n}{A^2} \qquad (4.5)$$

where $b' = b_g' + b_r'$ is the acceptable blur in the image. The first term is due to geometric optics, while the second term is due to diffraction from Rayleigh's criteria. Since Equation (4.5) must always be positive, the acceptable geometric blur must be larger than the Airy disk. Note that even when the object is in perfect focus ($\Delta_T = 0$), there is still a small amount of blurring due to diffraction. For example, the parameters for the microscope used in the experiments are *n*=1.5, $\lambda$=0.6 microns, *A* =0.42, and *m*=6.9. The resulting image blur due to diffraction (Airy disk diameter) is 12.026 microns. If the acceptable image blur is 12.45 microns (approximately 1 pixel on a 1/3 inch format CCD), then $\Delta_T = 0.22$ microns. Therefore, two points separated by *b'/m* or 1.8 microns will become indistinguishable if the points are moved as little as 0.11 microns out of the focal plane!

The next problem is how to generate synthetic images which account for the geometric depth of field and the Fraunhoffer diffraction. Using Fourier optics [28], a stationary linear optical system with incoherent lighting is described in terms of a 2D convolution integral:

$$I_{im}(x', y') = \iint I_{obj}(x, y) S(x - x', y - y') dx dy \qquad (4.6)$$

where $I_{im}(x', y')$ is the image intensity, $I_{obj}(x, y)$ is the object intensity, and *S(x,y)* is the impulse response or point spread function. This convolution is more efficiently computed using Fourier Transforms:

$$\tilde{I}_{im}(u, v) = \tilde{I}_{obj}(u, v) \tilde{S}(u, v) \qquad (4.7)$$

where the tilde represents the 2D Fourier Transform of the function, and *u* and *v* are spatial frequencies in the *x* and *y* directions.

Considering only the geometric depth of field, the impulse response is

$$S_g(r',\theta') = \begin{cases} \dfrac{4}{\pi(b_g')^2} & r' \le b_g'/2 \\ 0 & r' > b_g'/2 \end{cases} \tag{4.8}$$

where $r'$ is the radial distance for the impulse location in the image plane. The impulse response is radially symmetric about the impulse location and independent of $\theta'$. This implies that a geometrically defocused image is the focused image convolved with a filled circle of diameter $b_g'$.

Considering only Fraunhoffer diffraction, the impulse response is

$$S_d(r',\theta') = \pi^2 a^4 \left| \frac{2J_1\left(\dfrac{2\pi a r'}{\lambda f m}\right)}{\dfrac{2\pi a r'}{\lambda f m}} \right|^2 \tag{4.9}$$

where $J_1(\bullet)$ is the first order Bessel function, $a$ is the aperture radius, $\lambda$ is the wavelength of light, and $f$ is the focal length of the lens. This function is also radially symmetric about the impulse location and independent of $\theta'$. In addition, it is the expression used to generate the Airy disk. It would be computationally expensive to convolve this expression with the original image without the use of Fourier Transforms. Fortunately, there exists a simple expression in the Fourier domain. With incoherent light, the Fourier Transform of the impulse response is given by the autocorrelation of the aperture (pupil) function with its complex conjugate:

$$\tilde{S}_d(u,v) = \iint P^*(x,y)P(x+\lambda z'u, y+\lambda z'v)dxdy \tag{4.10}$$

For a circular aperture of radius $a$, the pupil function is

$$P(r_{uv},\theta) = \begin{cases} 1 & r_{uv} \le a \\ 0 & r_{uv} > a \end{cases} \tag{4.11}$$

and the resulting transfer function is given by

$$\tilde{S}_d(r_{uv}) = 2a\left[ a\sin^{-1}\left(\sqrt{1-\left(\frac{r_{uv}}{2a}\right)^2}\right) - \frac{r_{uv}}{2}\sqrt{1-\left(\frac{r_{uv}}{2a}\right)^2} \right] \tag{4.12}$$

where $r_{uv}$ is the radius in image frequency.

The combined impulse response of both the geometric depth of field and the Fraunhoffer diffraction is given by the convolution of $S_g$ and $S_d$, or in the frequency domain, the product of $\tilde{S}_g$ and $\tilde{S}_d$. It should be noted that both $S_g$ and $S_d$ act as low pass filters on the image. $S_g$ becomes the more dominant filter as the object is moved out of the focal plane. A block diagram of the entire synthetic image generation process is given in Figure 4.3.

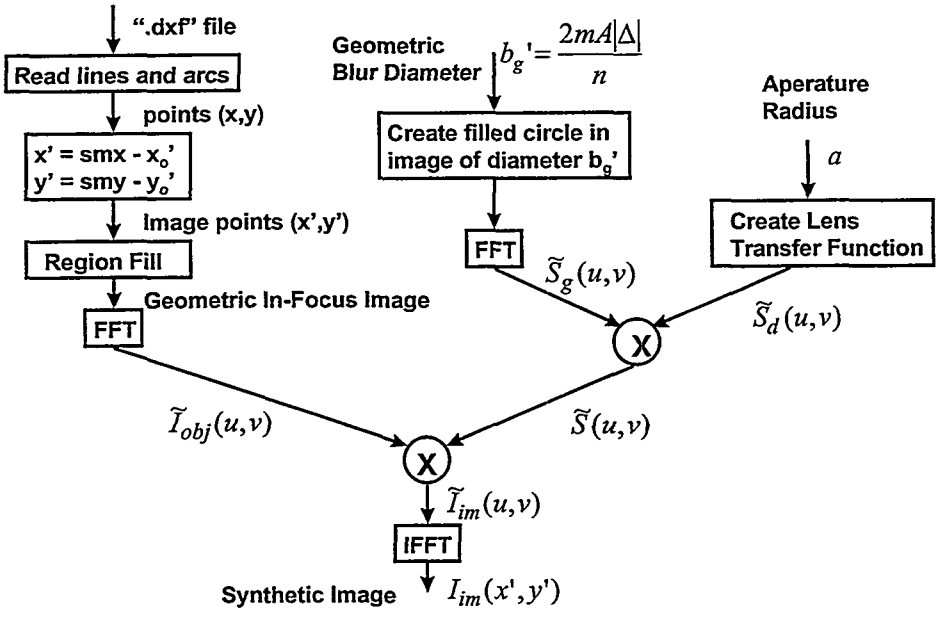


*Figure 4.3. Block diagram of synthetic image generation.*

Synthetically generated examples of Fraunhoffer diffraction and geometric blur are shown in Figures 4.4-4.6. Figure 4.4 shows the geometric and out-of-focus images of a 100 micron gear. Figure 4.5 shows a cross section of the geometric image and the same image after Fraunhoffer diffraction. Notice how the edges of the gear are rounded. Figures 4.6 shows a cross section of the image which is out-of-focus. The geometric blur becomes the dominant effect as the out-of-focus distance increases.

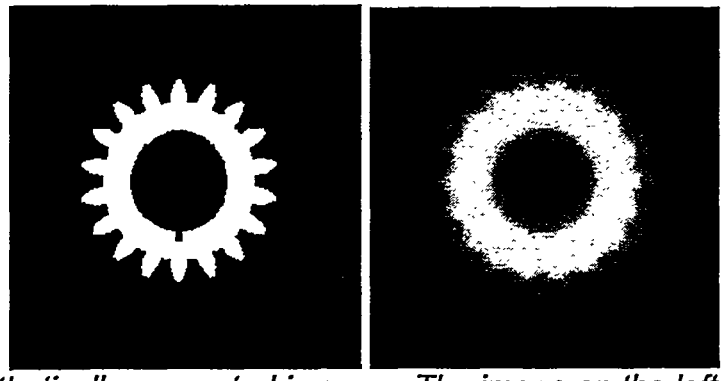

*Figure 4.4. Synthetically generated images. The image on the left is in-focus. The image on the right is a diffracted image which is 25 microns out of depth of field.*

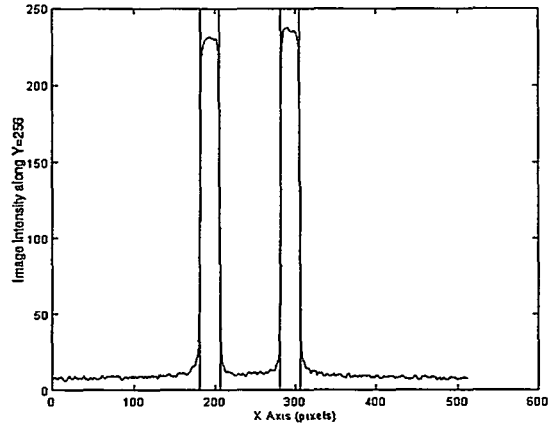


*Figure 4.5. Cross section of geometric in-focus image (vertical lines) and diffracted in-focus image.*

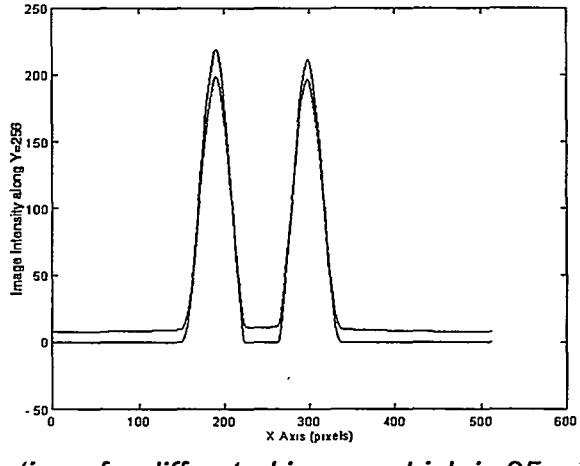


*Figure 4.6. Cross section of a diffracted image which is 25 microns out of depth of field. The cross section due only to geometric blurring is the curve which starts at zero and has peaks at 225. When diffraction is included, the image does not start at zero and the peaks are attenuated.*

These results can be compared to real images of a 100 micron gear under a microscope as shown in Figures 4.7 and 4.8. Figure 4.7 shows an image of the gear when in-focus, and when moved out-of-focus by 30 microns. Figure 4.8 shows a cross section of the in-focus and out-of-focus images. Notice that the edges of the in-focus image are rounded. Also, notice that the intensity of the out-of-focus image is attenuated and the slope is more gradual than the in-focus image. These results were predicted by the synthetic image (see Figures 4.4-4.6). However, the comparison also highlights some effects which are not yet modeled. In particular, the through-the-lens lighting is not uniform, and there are shadowing effects inside the gear. Also, the above analysis is only valid for parts which are all in the same z plane. Nevertheless, we can use this synthetic image to derive reference features for visual servoing, as will be shown next.

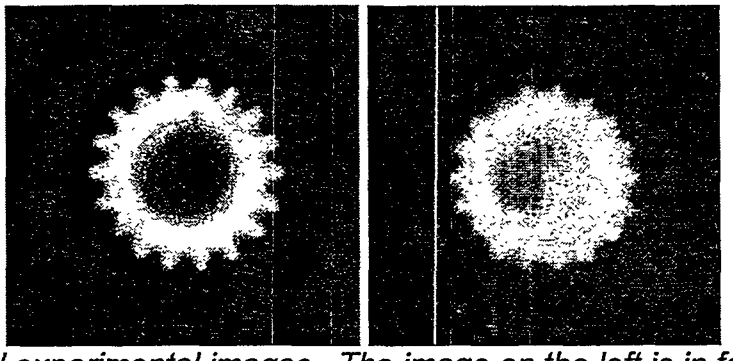

*Figure 4.7. Real experimental images. The image on the left is in focus. The image on the right is an image which is 30 microns out of depth of field.*

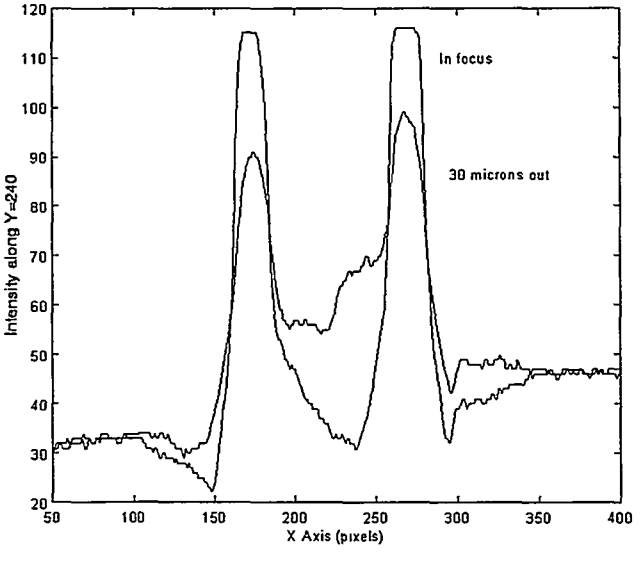


*Figure 4.8. Cross section of in-focus and out-of-focus images in Figure 4.7.*

## 4.2 Visual Servoing

As pointed out in [19], there are two ways in which to perform visual servoing: position-based and image-based. We are using the image-based approach. In this approach, the inverse image Jacobian is need to transform the differential motion in image coordinates into differential motion in the camera coordinates. The differential motion in the camera coordinates is, in turn, transformed to either robot end-effector or stage coordinates via another constant Jacobian relationship.

Since we are only interested in 4 DOF motion, the forward Jacobian of a single image point is a 2x4 matrix. Differentiating Equation (4.1) and inserting the linear and angular velocities with respect to the camera frame, the image Jacobian relationship for a single image feature point is

$$\begin{bmatrix} \dot{x}' \\ \dot{y}' \end{bmatrix} = \begin{bmatrix} m & 0 & 0 & -y' \\ 0 & m & 0 & -x' \end{bmatrix} \begin{bmatrix} {}^c\dot{x} \\ {}^c\dot{y} \\ {}^c\dot{z} \\ {}^c\omega_z \end{bmatrix} \tag{4.13}$$

where $(\dot{x}', \dot{y}')$ is the velocity of the projected point in the image plane, $({}^c\dot{x}, {}^c\dot{y}, {}^c\dot{z})$ is the linear velocity of the actual point with respect to the camera coordinate frame, and ${}^c\omega_z$ is the rotational velocity of the actual point about the *z* axis of the camera coordinate frame. Notice that in this expression, the linear motion along the optical axis *z* can not be observed. However, we know from the previous section that motion along the optical axis can be observed from the blurred diameter of a point. Summing and differentiating the expressions for blur diameter in Equations (4.3) and (4.4) and combining the result with Equation (4.13), an augmented image Jacobian for a single point can be defined as

$$\begin{bmatrix} \dot{x}' \\ \dot{y}' \\ \dot{b}' \end{bmatrix} = \begin{bmatrix} m & 0 & 0 & -y' \\ 0 & m & 0 & -x' \\ 0 & 0 & \dfrac{2mA}{n} & 0 \end{bmatrix} \begin{bmatrix} {}^c\dot{x} \\ {}^c\dot{y} \\ \left|{}^c\dot{z}\right| \\ {}^c\omega_z \end{bmatrix} \tag{4.14}$$

where $\dot{b}'$ is the differential change in blur in the image plane. Since the motion along *z* is independent of the other degrees of freedom, we can solve for that separately.

$$\left|{}^c\dot{z}\right| = \frac{n}{2mA}\dot{b}' \tag{4.15}$$

One simple way to realize Equation (4.15) and bring the parts into focus is to take the gradient of successive images and move the part along the *z* axis until the sum of gradient values in the image is maximized. This gradient maximum occurs

when the blur is a minimum and the edges are sharp. This focusing process is essentially what camcorders do to automatically adjust their depth of focus.

To control orientation, two image points must be observed. The inverse least squares solution to Equation (4.13) is

$$\begin{bmatrix} {}^{c}\dot{x} \\ {}^{c}\dot{y} \\ {}^{c}\omega_z \end{bmatrix} = \left(J^T J\right)^{-1} J^T \begin{bmatrix} \dot{x}_1' \\ \dot{y}_1' \\ \dot{x}_2' \\ \dot{y}_2' \end{bmatrix} \quad \text{where} \quad J = \begin{bmatrix} m & 0 & -y_1' \\ 0 & m & -x_1' \\ m & 0 & -y_2' \\ 0 & m & -x_2' \end{bmatrix} \tag{4.16}$$

The subscripts of $x$ and $y$ denote either point 1 or 2; both of which are located on the same part.

Equations (4.15) and (4.16) together with a proportional gain can be used in a resolved rate control scheme [19] to control the position and orientation of the part as shown in the next section.

## 4.3 Off-line Assembly Planning

In this section, we show how a synthetic image can be used to test image processing routines and to generate reference image features for control. Much of our work has concentrated on developing an optics simulator and off-line image processing extractor which is used to generate an augmented assembly plan. In Figure 4.9, the bold boxes represent computer programs which process the data files in the remaining boxes. The off-line system reads in the task plan from one file and the boundary representation of the CAD part from the ".dxf" file. A synthetic image is generated using the Fourier Optics from which a variety of image processing routines are tested and image features are automatically selected for control [29].

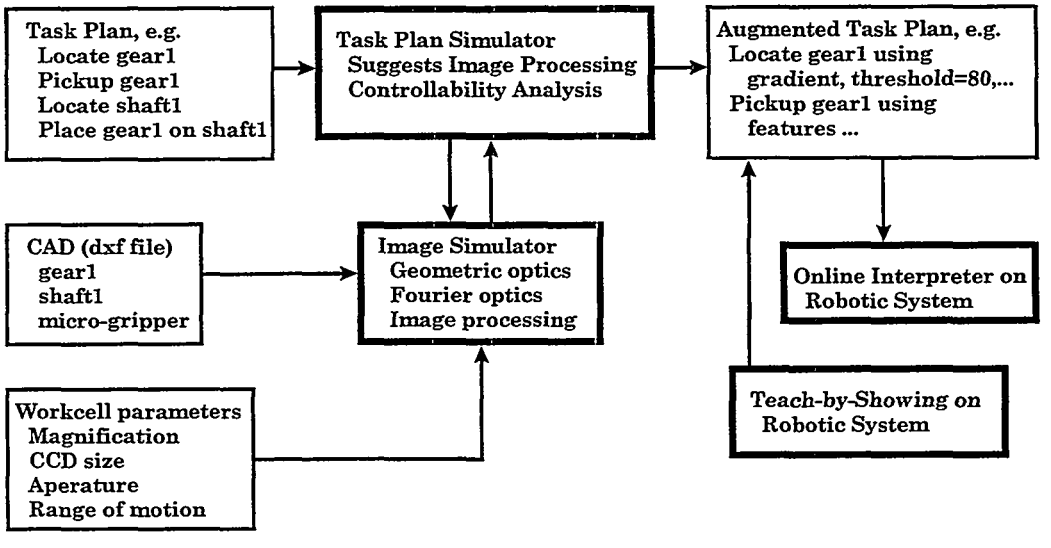


*Figure 4.9. Block diagram of CAD to assembly process.*

To date, we have successfully tested using a synthetic image to visually servo a LIGA gear to a desired x,y position. Figure 4.10 shows a sequence of images as the gear on the stage is visually servoed to the reference image position. Figure 4.10(a) shows the synthetic image which was generated from the CAD information. The part was recognized and located by finding the center of the part and then searching for 18 gear teeth on the outer diameter and a notch on the inner diameter. Its location in the image serves as the reference position. Figure 4.10(b) shows a real part as seen by the microscope and the application of the same image processing routines to locate the gear. Next, the part is visually servoed to the reference position at 30 Hz using the x,y centroid of the gear. Figure 4.10(c) shows the final position of the gear after visual servoing. Currently, the repeatability of the visual servoing is 1 micron in the x and y directions.

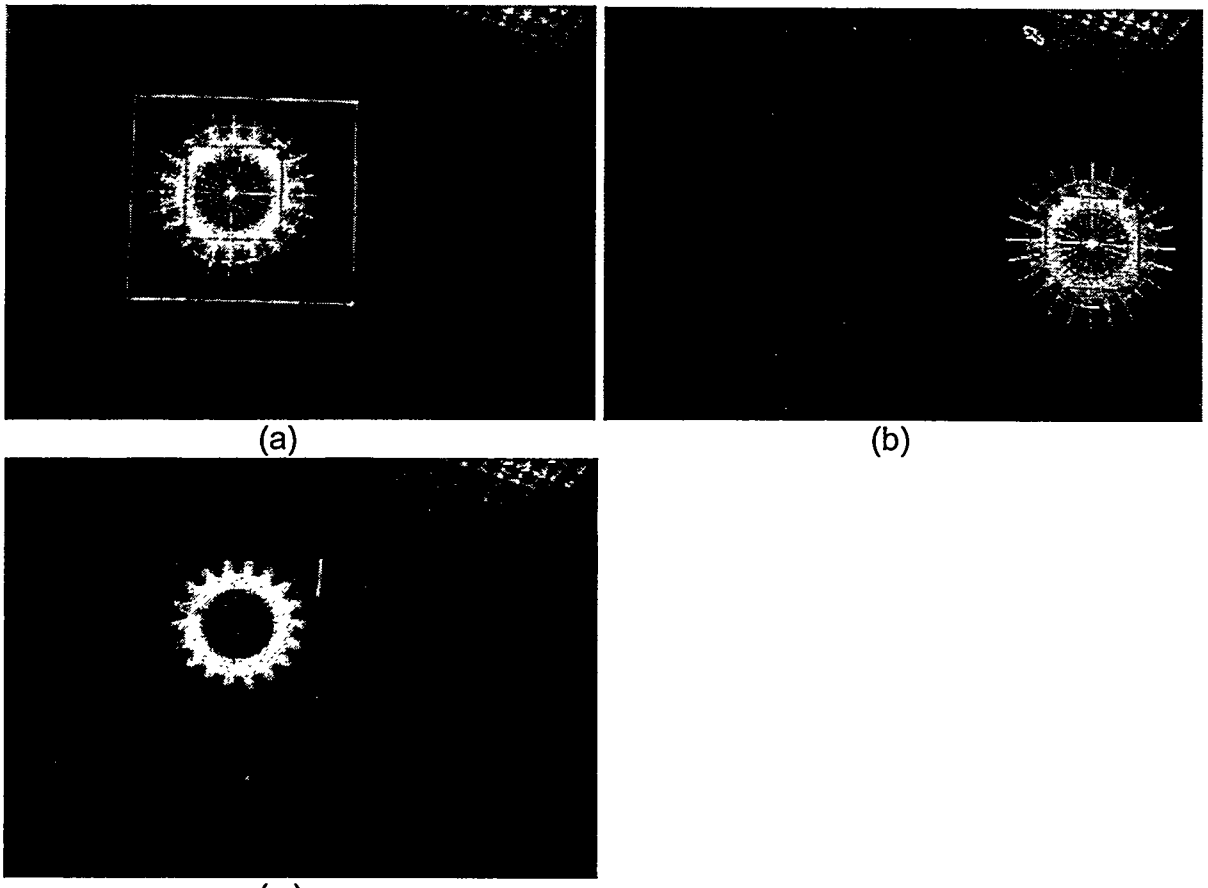


*Figure 4.10. Visual servoing experiment: (a) Synthetic reference image. (b) Initial location of real gear. ( c) Final position after visual servoing.*

## 5.0 Micro-assembly Planning

As discussed by [1][2], the relative importance of the interactive forces in microassembly is very different from that in the macro world. Gravity is almost negligible, while surface adhesion, electrostatic, and van der Waals forces dominate. Figure 5.1 illustrates typical problems associated with manipulation in the micro domain. It is typically easy to pick up parts, but very difficult to release parts because of these interactive forces. To some extent these problems can be reduced by cleaning parts and grounding contact surfaces. It may even be possible to design the microgrippers such that these forces are reduced [1]. But these forces can not be neglected, and an assembly plan must take these effects into account.

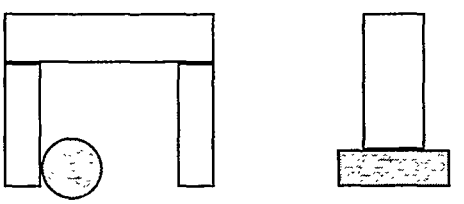

(a) (b)

*Figure 5.1. Micro domain problems: (a) Part adheres to one finger when the gripper opens. (b) Pneumatic probes require reversible pressure to "blow" the part away from the probe, thus releasing it.*

In the "lights out" micro-machine factory of the future, an engineer would develop a set of part and assembly models in a CAD package, and a computer program would generate the required tooling, fixturing, assembly sequence, path plan, and fine motion control parameters. Figure 5.2 shows the elements of a simple planning system. Bidirectional arrows are used to denote feedback between the elements. This feedback may be implemented as iterative trials from the search space of the task. More complex planning systems may have more interconnects between elements, but for simplicity of illustration Figure 5.2 will suffice. After the engineer designs the components and subassemblies, end-effectors and fixtures would be designed and then tested by an assembly planning module which would test geometric constraints between the components, end-effectors, and fixtures. The resulting assembly plan would be passed to a fine motion planning module which would modify the goal regions based on limitations in sensing and control. Finally, this modified motion plan would be sent to a motion planning module which would generate the final gross motions between goal and pre-image regions while avoiding obstacles in the environment.

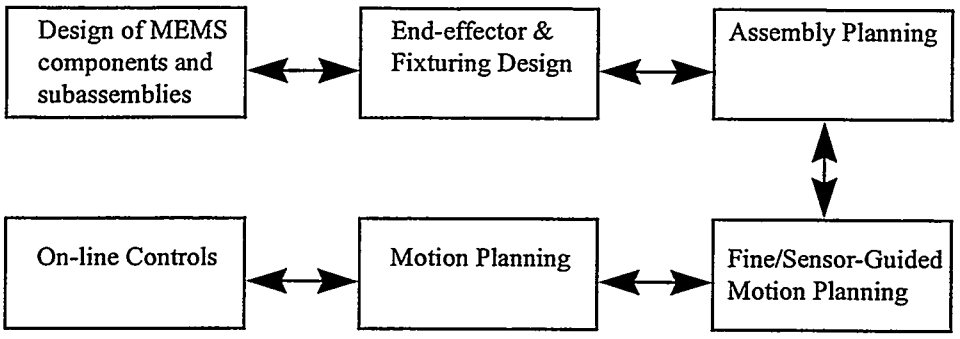


*Figure 5.2. Flow diagram of planning system for automated assembly of MEMS.*

Much research has been performed in assembly and path planning for the macro world [30], and it would be beneficial to directly apply this research where possible. In fact, the same flow diagram used in Figure 5.2 applies to the macro-world. So which elements need to be modified for the micro-domain? We believe that the assembly and motion planning modules in Figure 5.2 are unchanged in the micro-domain. The geometric constraints of the assembly planner will apply to the micro-domain as well as the free space path planning of the motion planner. However, fine motion planning and precise motion will differ from the macro-world cases, particularly when contact is involved. For example, the interactive forces in the micro-domain cause an assembly sequence not to be reversible. As pointed out in [3] (see Figure 5.3), reversing the motion used to pick up a part will generally not release it. The specification of goals is different and must be correctly modeled. In this section, we investigate how motion planning changes based on the interactive forces in the micro-domain.

In the next subsection, we provide background on the interactive forces which affect fine motion planning in the micro-domain. The following subsection uses these results to automatically generate a fine motion plan which is similar to that which was generated by a human operator in [3].

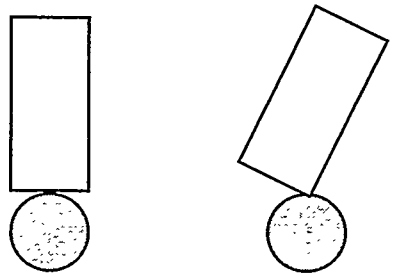


*Figure 5.3. In [3], the blunt end of a gold plated probe was used to pick up 2 micron diameter polymer particles and stack them inside an SEM. To release the particles, the probe was moved so that the edge of the probe contacted the particle, thus decreasing the contact area and reducing attractive forces.*

## 5.1 Interactive Forces

In this section, we describe two dominant interactive forces in the micro-domain: van der Waals and electrostatic. As mentioned in [1][2], surface tension also plays a dominant role in non-clean-room environments. In this paper, we will assume that the parts to be assembled are clean and that the humidity is low enough that surface tension effects can be neglected.

Throughout this section, we will consider the forces between a sphere and a rectangular block of different dimensions. The sphere represents the object being picked up, and the block represents the tool used to pick up the object. Previous works [1][2][31] have typically only considered the interactions between two spheres or between a sphere and an infinite half space. Unfortunately, these simple models can not be used to explain the motion sequence demonstrated in [3][4], where a tilting of the tool during part release is used to reduce the attractive forces to the object. In this paper, we strive to understand how to model this interaction and how this model can be used to plan assembly motions.

### *5.1.1. Van der Waals Force*

Van der Waals (sometimes called London's or dispersion) force is caused by a momentary dipole moment between atoms resulting from interaction between electrons in the outermost bands rotating around the nucleus. This moment exists even for atoms which do not contain a permanent polarization. While the average distribution of electrons is uniformly distributed about the nucleus, the outermost electrons of one atom are inducing a dipole on the other atoms which in turn induce a dipole on still more atoms. An easy-to-read overview of van der Waals forces is given in [32].

The end result is that the interaction energy between two atoms or molecules is proportional to the inverse of the sixth power of distance between the molecules.

$$E_i = -\frac{\lambda}{r^6} \tag{5.1}$$

where $r$ is the distance between the molecule centers and $\lambda$ is a constant. This constant depends on temperature and material properties such as the distortion polarization, permanent dipole moment, and ionization energy.

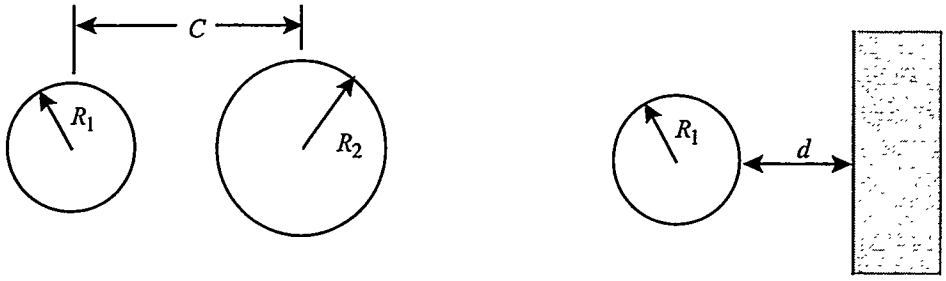


(a) (b)

*Figure 5.4. Notation for (a) two spheres, (b) sphere and half space.*

Hamaker [33] computed the non-retarded interaction energy and force between two macroscopic spheres (see Figure 5.4a). The energy of interaction between two particles containing *n* atoms per cm$^3$ is given by

$$E = -\int_{V_1}\int_{V_2} \frac{n^2\lambda}{r^6} dv_2 dv_1 \tag{5.2}$$

where $V_1$ and $V_2$ are the volumes of the first and second particles. Integrating the volume of two spheres, Hamaker found that the energy is given by

$$E_{vdwoo} = \frac{-H}{12}\left[\frac{R_1R_2}{C^2-(R_1+R_2)^2} + \frac{R_1R_2}{C^2-(R_1-R_2)^2} + 2\ln\frac{C^2-(R_1+R_2)^2}{C^2-(R_1-R_2)^2}\right] \tag{5.3}$$

where $R_1$ and $R_2$ are the radii of the two spheres, C is the distance between centers, and $H = \pi^2 n^2 \lambda$ is the Hamaker constant. The subscript *vdwoo* stands for van der Waal between two spheres. The corresponding force between two spheres is determined by taking the partial derivative with respect to C.

$$F_{vdwoo} = \frac{HCR_1R_2}{3}\left[\frac{8R_1^2R_2^2 - \left[C^2-(R_1-R_2)^2\right]\left[C^2-(R_1+R_2)^2\right]}{\left[C^2-(R_1+R_2)^2\right]^2\left[C^2-(R_1-R_2)^2\right]^2}\right] \tag{5.4}$$

By letting $R_2$ go to infinity, Hamaker also determined the non-retarded energy between a sphere and an infinite half space. It is given by

$$E_{vdwo|} = \frac{-H}{6}\left[\frac{R_1}{d} + \frac{R_1}{d+2R_1} + \ln\frac{d}{d+2R_1}\right] \tag{5.5}$$

where d is the distance from the wall to the edge of the sphere. The subscript *vdwo|* stands for van der Waal between a sphere and a half space. The corresponding force is

$$F_{vdwo|} = \frac{2HR_1^3}{3d^2(d+2R_1)^2} \tag{5.6}$$

As pointed out in [32], the energy of the approximation (5.1) changes from an inverse sixth to an inverse seventh power law at separations greater than 10nm to 50nm. This retardation is explained when accounting for the time of travel of the polarization field as it travels from one atom to the next. As the distance increases, the time of travel approaches the lifetime of the instantaneous dipole of the original molecule. Instead of the induced fields being additive, they become subtractive, and the energy and force of interaction is reduced. Lifshitz [34] first explained this phenomena, and others have gone on to develop very detailed (and computationally intensive) models which include this "screening" effect between dipoles [35-38].

While these more detailed models are more accurate, they are difficult to compute for more complex particle shapes. Therefore, in this report we have chosen to compute the non-retarded energy and force between a sphere and a rectangular block. This provides an upper bound on the interaction forces which will exist in experimentation. More importantly, this upper bound gives us a qualitative feel for how van der Waals forces affects motion planning as described in the next section.

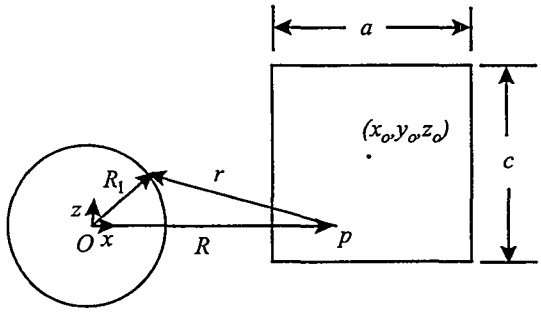


*Figure 5.5. Notation for computing van der Waals energy between a sphere of radius $R_1$ and a rectangular block centered at $(x_o, y_o, z_o)$ and of dimensions (a, b, c). The y direction at origin O is into the page.*

The derivation of energy between a sphere and a rectangular block follows that of Hamaker [33]. The energy of a particle *p* outside of the sphere is determined by integrating van der Waals energy inside the volume of the sphere with respect to the coordinates of *p* (see Figure 5.5).

$$E_p = -\int_{R-R_1}^{R+R_1} \frac{\pi\lambda n}{Rr^5}\left(R_1^2 - (R-r)^2\right)dr$$
$$= \frac{-\pi\lambda n}{12R}\left[\frac{2R_1}{(R+R_1)^3} + \frac{2R_1}{(R-R_1)^3} + \frac{1}{(R+R_1)^2} - \frac{1}{(R-R_1)^2}\right] \tag{5.7}$$

where $R_1$ is the radius of the sphere and $R$ is the distance from the center of the sphere to particle $p$. For a 2 micron diameter copper sphere, $E_p$ changes versus distance (either radial or tangential) as shown in Figure 5.6. Notice how energy decreases drastically versus radial distance as compared to the tangential distance. The same decrease in energy is seen over a radial change of 10 Angstroms as is seen over a tangential change of 1000 Angstroms.

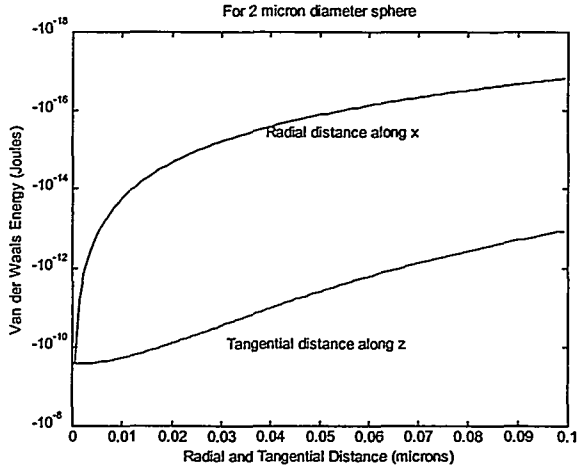


*Figure 5.6. Van der Waals energy between a 2 micron diameter copper sphere and a copper atom. Hamaker's constant for copper is 32.4676x10$^{-20}$ J. The minimum distance between the sphere and the atom is 4 Angstroms.*

The total energy between the sphere and a block is determined by integrating $E_p$ inside the block's rectangular volume.

$$E_{vdwob} = \int_{z_o-c/2}^{z_o+c/2} \int_{y_o-b/2}^{y_o+b/2} \int_{x_o-a/2}^{x_o+a/2} E_p n dx dy dz \tag{5.8}$$

where

$$R = \sqrt{x^2 + y^2 + z^2}\,.$$

The subscript *vdwob* stands for van der Waal between a sphere and a block. This expression is a difficult integral to evaluate symbolically, so we have opted to evaluate it numerically using Gauss-Legendre integration. Using 40 abscissa points, this integration is exact for all polynomials of degree 79 or less. The van der Waals force along the x, y, and z axis is given by

$$F_l = \frac{\partial F}{\partial l} = \int_{z_o-c/2}^{z_o+c/2} \int_{y_o-b/2}^{y_o+b/2} \int_{x_o-a/2}^{x_o+a/2} \frac{\partial E_p}{\partial R}\frac{\partial R}{\partial l} n dx dy dz, \quad l = x, y, z \tag{5.9}$$

where

$$\frac{\partial E_p}{\partial R} = \frac{\pi \lambda n}{4R^2}\left[\frac{2RR_1}{(R+R_1)^4} + \frac{2RR_1}{(R-R_1)^4} + \frac{1}{(R+R_1)^2} - \frac{1}{(R-R_1)^2}\right] \quad \text{and} \quad \frac{\partial R}{\partial l} = \frac{l}{R}.$$

This triple integral is also computed numerically using Gauss-Legendre integration.

Figure 5.7 shows the van der Waals force between a 2 micron diameter copper sphere and a 1 $\mu m^3$ copper block as the block moves away from the sphere in the *x* direction. As a comparison, the van der Waals force between a sphere and a half space as given in Equation (5.6) is also shown. Note that the van der Waals force between the sphere and block is less than that between a sphere and half space when the two objects are touching. As the block moves away from the sphere, the sphere/half space and sphere/block forces are approximately equal when the objects are very close. As the block moves further away, the van der Waals forces for the sphere/block are less than for the sphere/half space. These results are intuitively correct. It should also be noted that the gravitational force on a 2 micron diameter sphere of copper is $3.678093 \times 10^{-13}$ N. So the van der Waals force is the dominant force for separations less than 0.5 microns.

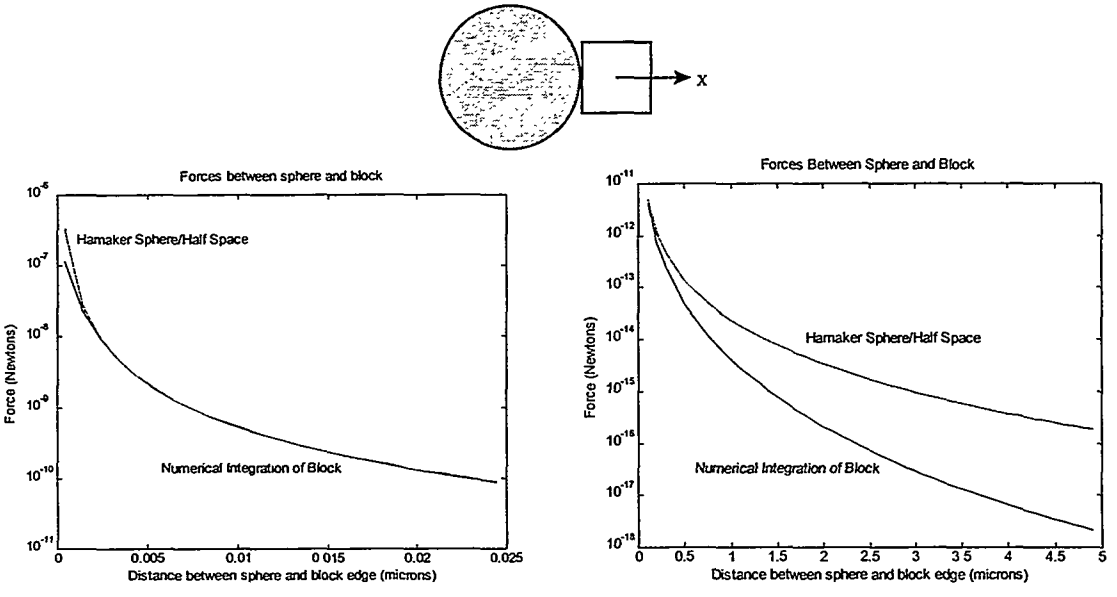


*Figure 5.7. Van der Waals force between a 2 micron diameter copper sphere and a 1 $\mu m^3$ copper rectangular block as the block is moved radially away from the sphere. For copper, the Hamaker constant is $H=32.4676 \times 10^{-20}$ Joules.*

Figure 5.8 shows the van der Waals force between the sphere and the block as the block is translated tangentially to the sphere in the *z* direction. Notice that the force remains relatively constant until the corner of the block reaches the edge of the sphere. At this point the force is one-half of the force when the block is centered on the sphere. As the block moves further along the tangential direction, the force decreases dramatically since the block is no longer in contact with the sphere.

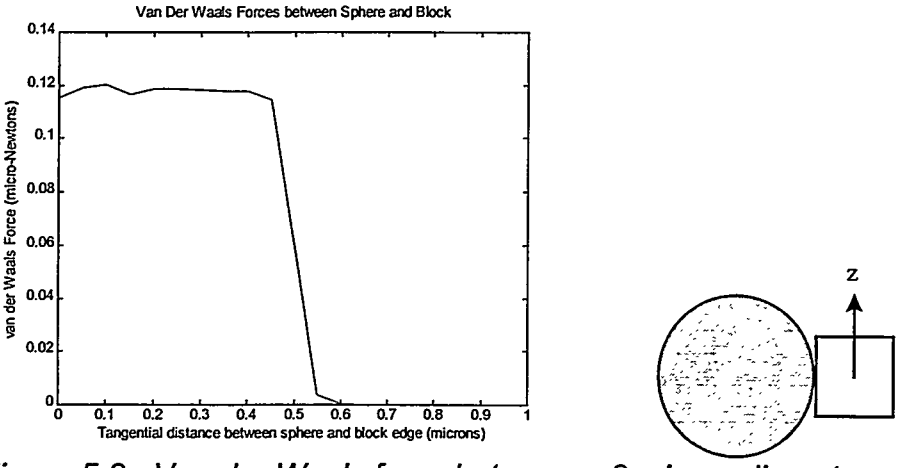


*Figure 5.8. Van der Waals force between a 2 micron diameter copper sphere and a 1 $\mu m^3$ copper rectangular block as the block is moved tangentially away from the sphere.*

Figure 5.9 shows the van der Waals force between the sphere and the block as the block is rotated with respect to the sphere. This is computed by moving the block in the x and z directions simultaneously so that a corner of the block is always touching the sphere (4 Angstroms away). Again, the force of interaction drops off as the block rotates to 45 degrees. From Figures 5.8 and 5.9, we can see that the minimum in-contact van der Waals force occurs when the block is touching the sphere on it's edge at 45 degrees. Because van der Waals force is very short range, this position of minimum in-contact force changes very little as the dimensions of the block change. As will be seen in the path planning section, this position of minimum in-contact force may be used to plan the release position of a grasp.

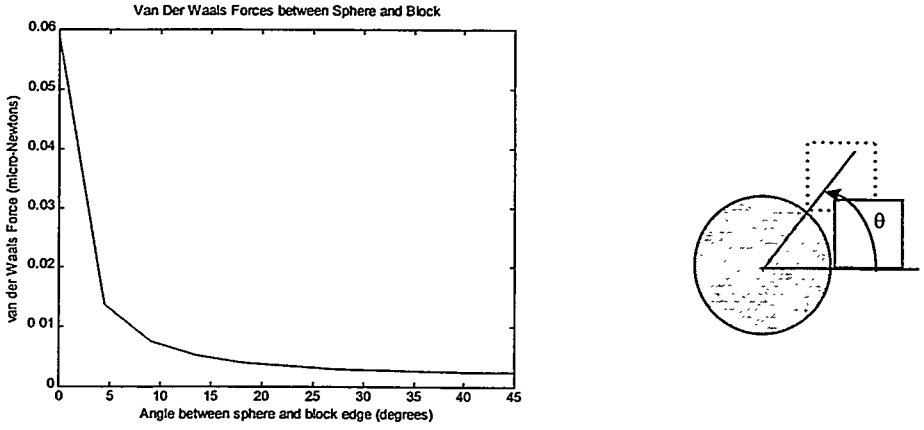


*Figure 5.9. Van der Waals force between a 2 micron diameter copper sphere and a 1 $\mu m^3$ copper rectangular block as the block is rotated around the sphere.*

### 5.1.2 Electrostatic Force

Now let us look at the second interactive force: electrostatic. We will only consider the electrostatic force between two conducting particles with a thin dielectric layer to insulate the two. As pointed out in [2], dielectric oxide layers of up to 1nm are possible after several days in air at room temperature. Again, we will compute the forces between a sphere and a rectangular block.

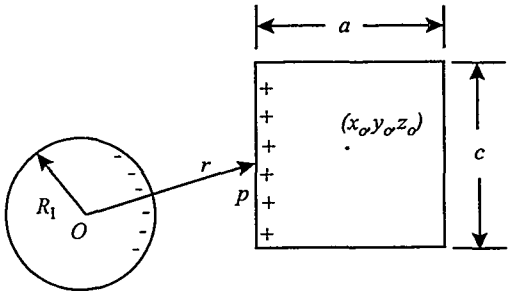


*Figure 5.10. Notation for computing electrostatic force between a sphere of radius $R_1$ and a rectangular block centered at ($x_o$, $y_o$, $z_o$) and of dimensions (a, b, c). The y direction at origin O is into the page.*

For a conductor, the electric field inside of the sphere and the block will be zero, and all electrostatic charge will reside on the surface (see Figure 5.10). Using Gauss's law, it can be shown that the electric field between a particle *p* and the sphere is given by [39]

$$\vec{E}_1 = \frac{Q_1}{4\pi\varepsilon_o r^2}\hat{r}, \quad r > R_1 \tag{5.10}$$

where

$$r^2 = x^2 + y^2 + z^2$$

$$Q_1 = 4\pi R_1^2 \sigma_1$$

*r* is the distance from the center of the sphere to the particle, $\hat{r}$ is the unit vector from the center of the sphere to the particle, $R_1$ is the radius of the sphere, $\sigma_1$ is the charge density of the sphere, and $\varepsilon_o$ is the permittivity of air ($8.85 \times 10^{-12}$ $C^2/(Nm^2)$). The infinitesimal force on a charge on the block's surface is given by

$$d\vec{F} = \vec{E}_1 \sigma_2 da_2 \tag{5.11}$$

where $\sigma_2$ is the charge density of the block and $da_2$ is the infinitesimal area of the block's surface. The force in the *x* direction on the side of the block closest to the sphere (see Figure 5.11) is

$$F_x\Big|_{x=x_o-a/2} = \int_{z_o-c/2}^{z_o+c/2}\int_{y_o-b/2}^{y_o+b/2} \sigma_2 E_1\Big|_{x=x_o-a/2} \frac{x_o - a/2}{\sqrt{\left(x_o - a/2\right)^2 + y^2 + z^2}}\, dydz$$
$$= \frac{R_1^2\sigma_1\sigma_2\left(x_o - a/2\right)}{\varepsilon_o} \int_{z_o-c/2}^{z_o+c/2}\int_{y_o-b/2}^{y_o+b/2} \frac{1}{\left[\left(x_o - a/2\right)^2 + y^2 + z^2\right]^{3/2}}\, dydz \qquad (5.12)$$

Similarly, the forces in the *y* and *z* directions on the side closest to the sphere are

$$F_y\Big|_{x=x_o-a/2} = \frac{R_1^2\sigma_1\sigma_2}{\varepsilon_o} \int_{z_o-c/2}^{z_o+c/2}\int_{y_o-b/2}^{y_o+b/2} \frac{y}{\left[\left(x_o - a/2\right)^2 + y^2 + z^2\right]^{3/2}}\, dydz \qquad (5.13)$$

$$F_z\Big|_{x=x_o-a/2} = \frac{R_1^2\sigma_1\sigma_2}{\varepsilon_o} \int_{z_o-c/2}^{z_o+c/2}\int_{y_o-b/2}^{y_o+b/2} \frac{z}{\left[\left(x_o - a/2\right)^2 + y^2 + z^2\right]^{3/2}}\, dydz \qquad (5.14)$$

In these expressions, the inner integral can easily be integrated analytically, but the outer integral is more complex, so it has been computed numerically. Similar expressions can be found for the forces exerted on the other five sides of the block. The total forces are given by

$$F_l = F_l\Big|_{x=x_o-a/2} + F_l\Big|_{x=x_o+a/2} + F_l\Big|_{y=y_o-b/2} + F_l\Big|_{y=y_o+b/2} + F_l\Big|_{z=z_o-c/2} + F_l\Big|_{z=z_o+c/2} \quad , \quad l = x, y, z \qquad (5.15)$$

Figures 5.11 and 5.12 show the force of electrostatic attraction for a 2 micron diameter sphere and a 1 $\mu m^3$ rectangular block, both with surface charge densities of $25 \times 10^{-6}$ C/m$^2$. As reported in [2], the breakdown strength of air is limited to a maximum charge density of about $30 \times 10^{-6}$ C/m$^2$ at atmospheric pressure. As the block moves away from the sphere in the *x* and *z* directions, the electrostatic force decreases. Because of symmetry, the force in the *y* direction is zero. Notice that the electrostatic force does not drop off as quickly as the van der Waals forces. This is because the electrostatic force is a longer range force.

Figure 5.13 shows the electrostatic force as the block is rotated with respect to the sphere. Again, the force of interaction drops off as the block rotates to 45 degrees. Similar to van der Waals forces, the minimum in-contact force occurs when the edge of the block is at 45 degrees to the sphere. However, since electrostatics is a longer range force, the minimum in-contact force is not at 45 degrees if the dimensions of the block change. For example, if the *x* dimension (*a*) is larger than the z dimension (*c*), then the minimum in-contact force will occur at less than 45 degrees.

These results will be used in the next section to determine the goal regions for picking up and releasing a sphere with a rectangular block gripper.

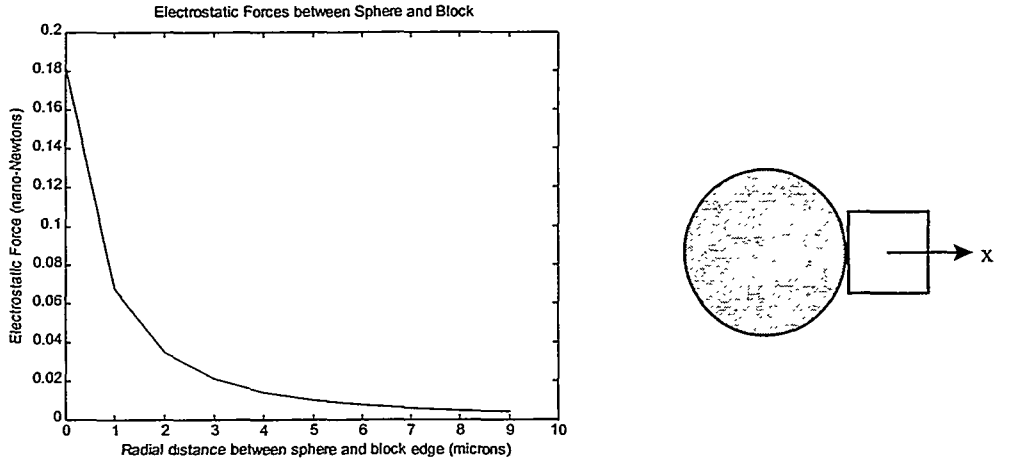


*Figure 5.11. Electrostatic force between a 2 micron diameter sphere and a 1 $\mu m^3$ rectangular block as the block is moved radially away from the sphere. The surface charge density of both the sphere and block are $25x10^{-6}$ $C/m^2$. Minimum separation is 4 Angstroms.*

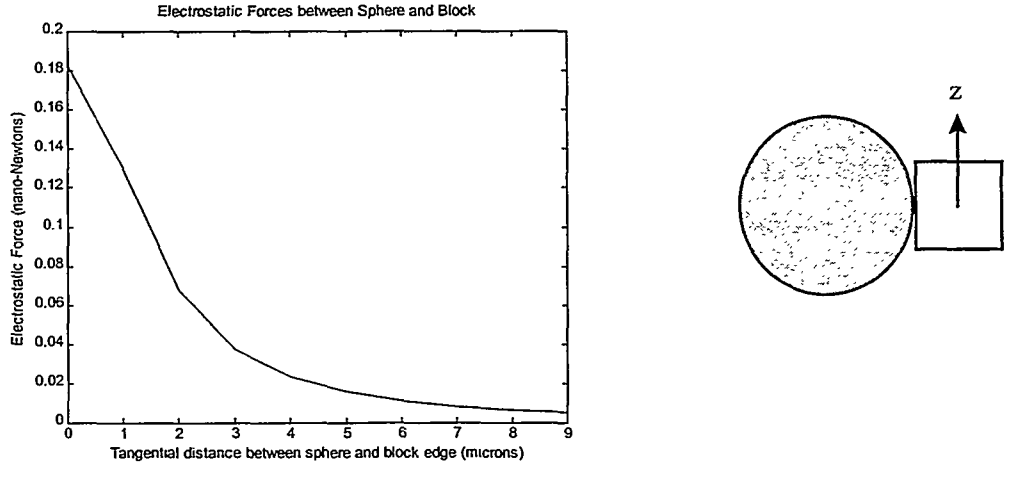


*Figure 5.12. Electrostatic force between a 2 micron diameter copper sphere and a 1 $\mu m^3$ copper rectangular block as the block is moved tangentially away from the sphere. Minimum separation in the x direction is 4 Angstroms.*

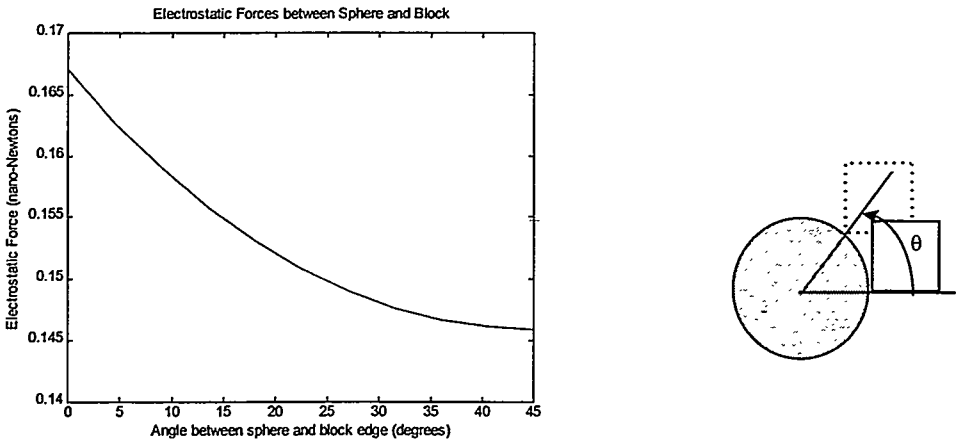


*Figure 5.13. Electrostatic force between a 2 micron diameter copper sphere and a 1 $\mu m^3$ copper rectangular block as the block is rotated around the sphere. Minimum separation is 4 Angstroms.*

## 5.2. Path Planning

Considerable research has been performed in motion planning and is summarized in [30]. As mentioned in the introduction, we believe that much of the work developed for the macro-world will directly apply to the micro-domain except where performing fine motion control. One example where macro-world fine motion planning is not acceptable in the micro-domain is compliant motion. While [41-45] showed that compliant motion may be used to expand the acceptable motion control uncertainty for peg-in-hole insertions and other placement tasks in the macro-world, this is not desirable in the micro-domain. First, compliant motion in the micro-domain generates particles on the rubbing surfaces which further complicate the assembly. Second, the friction cone on micro-surfaces will be enlarged because of the dominant van der Waals and electrostatic forces mentioned in the previous sections.

Another example of where macro-world fine motion planning needs to be modified for the micro-domain is fine motion vision planning as described in [23]. In the macro-world, simple geometric optics have been used for fine motion planning where vision is used as a feedback sensor. In the micro-domain, the size of the parts approach the wavelength of light, and complex nonlinear optics are needed to predict the effects of Fraunhoffer diffraction on the image processing [24]. This result will require that all fine motion control must occur in the very narrow depth of field of the microscope optics. This is an area of future research.

In this section, we will investigate how the force relationships presented in the previous section affects fine motion planning with force sensing. In particular, we will concentrate on the simple pick-up and release of a spherical particle with a rectangular block shaped tool. For simplicity, we will only consider motion planning in the $x$, $z$, and $\theta$ space as shown in Figure 5.14.

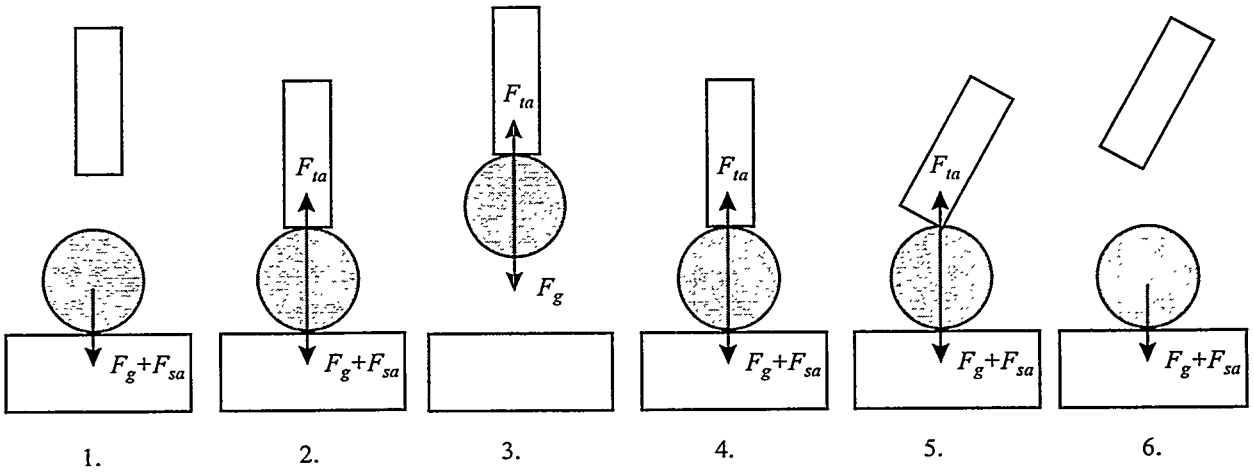


*Figure 5.14. Steps to pick up and release a sphere with a flat-tipped tool assuming only van der Waals forces and no electrostatic forces. Between steps 4 and 5, a rolling contact is assumed.*

The static forces acting on the sphere at the various stages of pick up and release are the force of gravity $F_g$, the force of surface attraction $F_{sa}$, and the force of tool attraction $F_{ta}$. To pick up the part, the force of tool attraction must be greater than the gravitational force and the force of surface attraction. To hold the part, the force of tool attraction must be greater than the gravitational force. Finally, to release the part, the force of tool attraction must be less than the gravitational force and the force of surface attraction. In summary,

$$\begin{aligned} F_{ta} &> F_g + F_{sa} && \text{to pick up part} \\ F_{ta} &> F_g && \text{while holding part} \\ F_{ta} &< F_g + F_{sa} && \text{to release part} \end{aligned} \qquad (5.16)$$

For ease of illustration, assume that both the sphere and the tool tip are made of copper, and there is no electrical charge on either the sphere, tool, or assembly surface. In other words, electrostatic forces are negligible. Initially, the sphere is resting on a surface of a different material. If the resting surface were also of copper, we would not be able to pick up the sphere with a flat tipped tool. The force of gravity acting on the sphere is given by

$$F_g = \frac{4}{3}\pi R_1^3 \rho g \qquad (5.17)$$

where $R_1$ is the radius of the sphere, $\rho$ is the density of the material, and $g$ is the gravitational acceleration. For a 2 micron diameter sphere of copper, $F_g = 3.678093\text{x}10^{-13}$ N. The force of attraction between the sphere and the surface is given by Equation (5.6). In certain cases, the equivalent Hamaker constant for two different materials is given by

$$H_{12} = \sqrt{H_1 H_2} \tag{5.18}$$

where $H_1$ and $H_2$ are the Hamaker constants for the individual materials. If the resting surface is made of a aluminum ($H_2$= 3.43774x10$^{-20}$ Joules), then the composite Hamaker constant is $H_{12}$= 10.5648x10$^{-20}$ Joules. Assuming a 4 Angstrom separation and the same 2 micron diameter copper sphere considered in the previous section, the van der Waals force between the copper sphere and the aluminum surface is $F_{sa}$ = 0.110 μN. Assuming that the tool has the same dimensions as the 1 μm$^3$ copper block considered in the previous section, the force of tool attraction is $F_{ta}$ = 0.116 μN when the tool is centered over the sphere. When the tool is moved so that one edge is on the surface of the sphere, the force of tool attraction becomes $F_{ta}$ = 0.059 μN. When the tool is tilted at 45 degrees, the force of tool attraction decreases to $F_{ta}$ = 0.025 μN.

For the values of $F_{ta}$, $F_g$, *and* $F_{sa}$ mentioned above, the tool will be able to pick up the sphere by centering the tool over the sphere. As seen in Figure 5.8, the force of tip attraction stays fairly constant over the width of the tip (approximately 1 μm). Because the gravitational forces are so small, the tool will be able to hold the sphere even when in the minimum in-contact position (the edge of the probe is at 45 degrees to the sphere). To release the sphere, the tool must be moved to the edge of the sphere. In this particular case, the tool will not have to be tilted to further reduce $F_{ta}$. In other cases where the surface material changes or the size of the sphere and tool change, the tool may have to be tilted to further reduce $F_{ta}$.

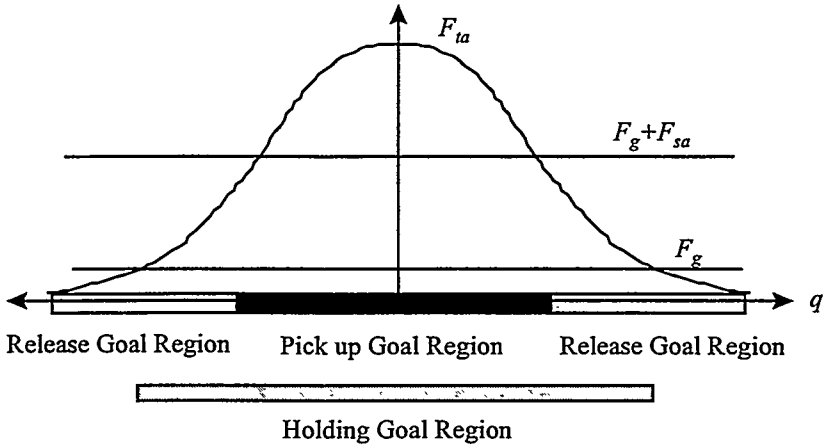


*Figure 5.15. Release, pick up, and holding goal regions in configuration space are determined from the interactive forces in the micro-domain.*

In general, Equation (5.16) together with the equations for attractive forces described in the previous section can be used to classify the various goal regions in configuration space [25]. Once the pick-up, holding, and release goal regions are determined, normal assembly and path planning routines can be used to determine assembly sequences and collision-free path plans. Figure 5.15 shows a one-

dimensional plot of attractive tool force versus the configuration $q$. In the example above, configuration $q$ is a three-dimensional space including the $x$ and $z$ position and orientation of the tool. A planning routine must search this space while the tool contacts the part and classify the goal regions using Equation (5.16). This search is not as difficult as it first appears since the dimension of the search space is greatly reduced by the in-contact (within say 4 Angstroms) constraint between the tool and the part. If the user-specified goal region of the sphere is chosen to be a single point on the arc and the user-specified goal region on the tool is the bottom line segment excluding the end points (see Figure 5.16a), then the search space reduces to a 1 dimensional search along a tangent line segment (as was performed in Figure 5.8). The line segment of the tool must be tangent to the sphere at the user-specified goal point on the sphere; otherwise, the tool will penetrate the sphere.

If the end points of the tool edge are included in the user-specified goal region on the tool, the tool may freely rotate about the end-point where the tool contacts the sphere. The range of rotation is 180 degrees minus the angle between the tool goal region and the adjacent line segment of the tool. When the end-points are included, a 1 dimensional rotational search at both end-points will be required as shown in Figure 5.9. The time complexity of the problem is $O(n+2m)$ where $n$ is the discretization along the tool line segment and $m$ is the discretization in angular rotation at the end-points.

The dimensions of the search space increase if the user-specified goal region on the sphere is an arc segment instead of a single point (see Figure 5.16b). The time complexity of the problem becomes $O(n^2+2mn)$ where the same discretization $n$ is used along the arc of the sphere and the line segment of the tool.

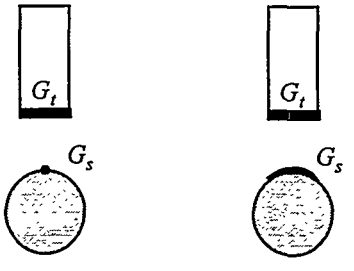


*Figure 5.16. User-specified goal regions on the tool $G_t$ and on the sphere $G_s$. User-specified goal region on the tool is a line segment. (a) User-specified goal region on the sphere is a single point. (b) User-specified goal region on the sphere is an arc.*

## 6.0 Parallel Assembly of LIGA

When developing MEMS, there are three primary technologies: surface micromachined silicon, bulk micromachined silicon, and LIGA. All three technologies have their own advantages and disadvantages. For instance, the surface and bulk micromachined silicon technologies take advantage of the infrastructure and machinery developed for producing integrated circuits [46]. This infrastructure has been designed for massively parallel fabrication, where hundreds of identical copies of the same device are replicated on a single silicon wafer. On the downside, this same infrastructure limits the types and thickness of materials, and the design of these devices. Typically, silicon-based materials are used. Also, the devices are typically designed to be planar, although pop-up three-dimensional structures have been demonstrated [47].

LIGA is an alternative technology, where the component sizes typically lie between conventionally machined components and surface micromachined silicon components [48][49]. The advantages of the LIGA approach are that the individual piece parts can be fabricated out of metals and plastics, and they are typically thicker than surface micromachined parts. Although the parts are typically limited to stepwise prismatic shapes, the parts can be assembled into complex, three-dimensional structures, which is a requirement for high aspect ratio (height-to-width) precision micro-scaled components. Unfortunately, this assembly step is a time consuming, labor intensive process, which greatly limits the mass production of the LIGA devices.

In the past, many researchers have investigated the assembly of individual MEMS components with teleoperated robotic devices [3-7][50]. More recently, semi-automated assembly systems with vision and force feedback have been developed [51-54]. However, all of these systems only manipulate individual components. In the future, for LIGA to be more widely accepted as an analogous process to planar microfabrication, a means of batch manufacturing is needed [55][56]. Similar to the parallel fabrication process of silicon surface machined devices, LIGA-fabricated MEMS need to be fabricated and assembled using "standard" processes that are parallel in nature. In this section, we investigate the assembly of parallel LIGA parts and the use of multiple cameras for visual feedback.

As an example, imagine building 100 LIGA-fabricated transmissions in parallel. For a geared transmission to be formed, multiple layers of LIGA gears would have to be bonded together and released onto pins (see Figure 6.1). Sandia National Laboratories has shown that it may be possible to do this by using diffusion bonding to adhere layers of LIGA parts [57]. The "standard" processes would consist of four steps: fabrication, assembly, diffusion bonding, and release. These steps would be repeated several times, each time adding a new layer of LIGA to the final assembly. The fabrication step is the standard LIGA process of developing a PMMA (polymethylmethacrylate) mold using X-ray lithography, electroplating the metal on the wafer, and removing the PMMA mold, thus leaving the LIGA layer on the wafer.

The assembly step consists of aligning and mating two LIGA layers on two separate wafers. The diffusion-bonding step adheres the new layer of LIGA to a previous layer of LIGA. The release step chemically etches the thin sacrificial layer of the top wafer, thus releasing this LIGA layer. In this section, we will discuss in detail only the assembly step. The details of the other two steps are still being actively pursued.

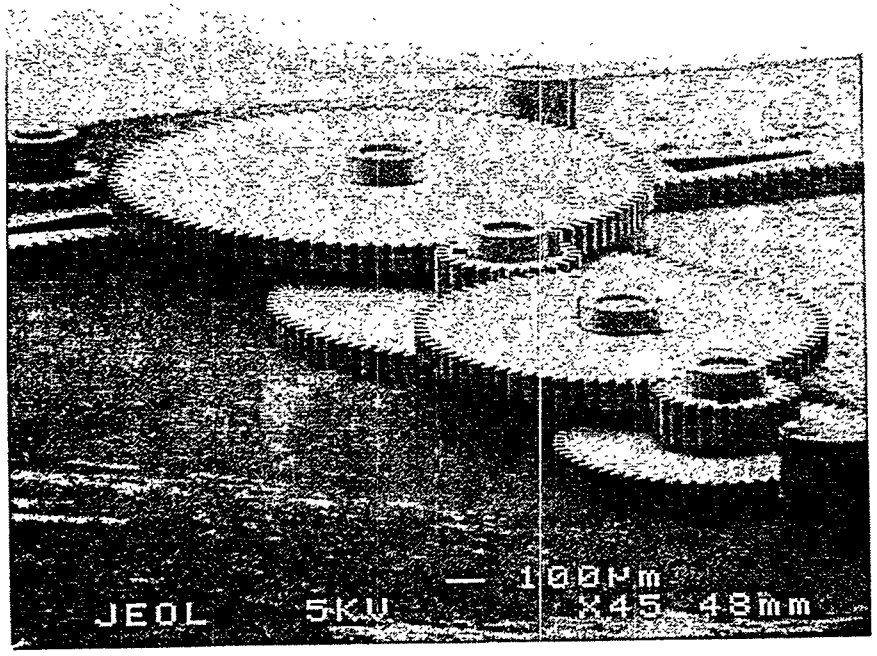


*Figure 6.1. Geared transmission made of LIGA parts.*

## 6.1 Parallel Assembly Workcell

During FY98, we designed, fabricated, and tested a workcell which presses 386 micron and 485 micron diameter pins into a LIGA substrate and then places a 3-inch diameter wafer with LIGA gears on the pins. Two microscopes are used to locate holes in the LIGA substrate, pins to be pressed in the holes, and gears to be placed on the pins. We have demonstrated that the vision system can locate parts within 3 microns. Our AMTI manipulator can then place the parts within 0.4 microns repeatability.

Figures 6.2 and 6.3 show the lay-out of our parallel assembly system. A pallet under the AMTI robot holds three 3-inch diameter silicon wafers. The wafer in the middle has a LIGA substrate bonded to it. This substrate contains 382 micron and 481 micron diameter holes. The wafer to the left contains 386 and 485 micron pins,

which have been manually placed in clearance holes (392 and 492 microns). The wafer to the right is upside down and contains LIGA gears (with 394 and 496 clearance holes) still bonded to the plating material on the wafer. The robot first picks up the pins from the wafer on the left, press fits them into the wafer in the middle, and then places the wafer on the right onto the wafer in the middle such that the pins and gears align. The resulting wafer sandwich would then be taken to a chemical bath where the thin metal sacrificial layer on the top wafer would be removed, thus releasing the gears. The gears would then be free to rotate on the press-fit pins.

Three tools are mounted on the toolplate of the AMTI robot. The first is a dial gage, which is used to align the surface of the pallet with the AMTI *x,y* plane. The second tool is a pin insertion tool, which contains a vacuum tip for picking up a pin and a vertical pneumatic actuator for pressing the pin to a specified force. The third tool is a vacuum chuck for picking up and placing the wafer of gears onto the wafer of inserted pins.

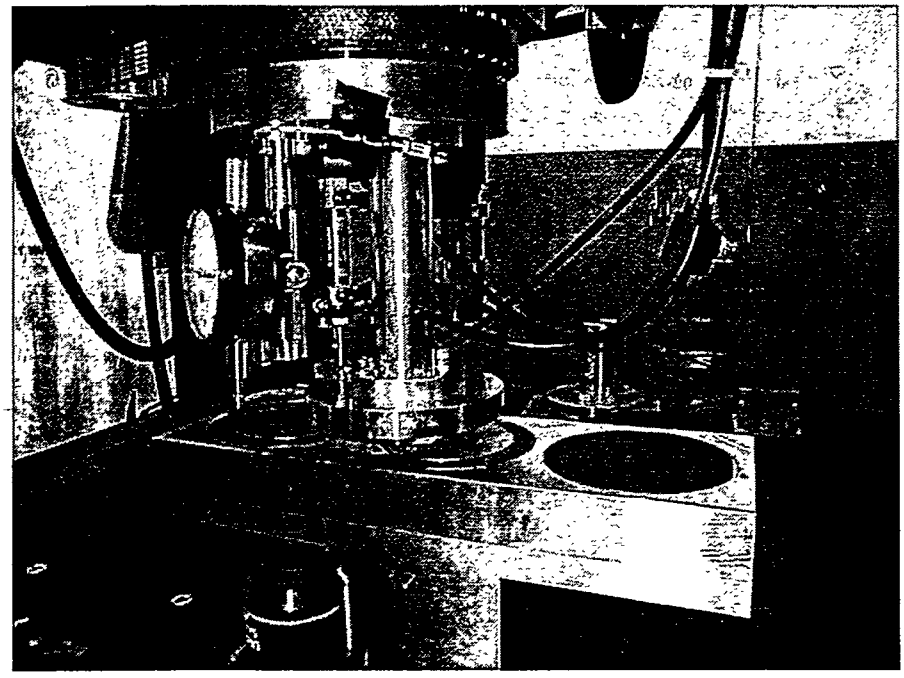

*Figure 6.2. Parallel assembly lay-out used to insert pins and align wafers. The upward looking microscope is visible in the lower left of the picture.*

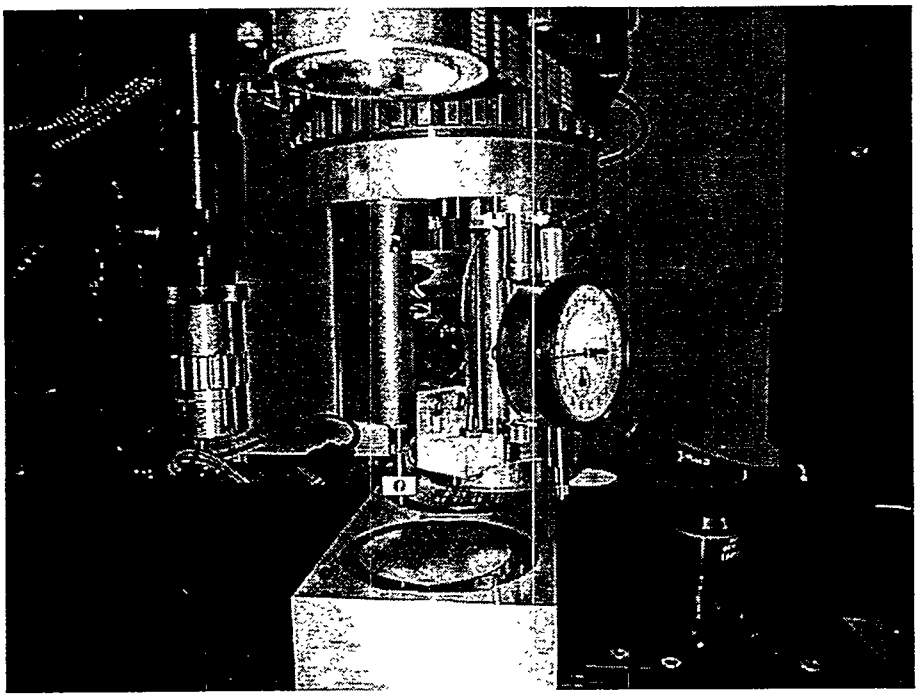

*Figure 6.3. Perpendicular view of parallel assembly lay-out. Downward looking microscope is on the left side of the picture, and the upward looking microscope is on the right.*

## 6.2 Vision System Calibration

Calibration of the vision system is key to the localization and alignment of the pins and gears. The exact locations of the pins, gears, pin insertion tool, and wafer-handling tool are not known *a priori*. Instead, we use the vision system to determine these locations.

A 3-inch diameter calibration wafer is used to calibrate both the downward and upward looking microscope cameras. This ceramic wafer has two metal pins that have been bonded into the wafer, perpendicular to the surface. The result is that two small circular holes (147 and 244 microns diameter and 488 microns apart) are visible on both sides of the wafer. Originally, we had planned to use the difference in size of the two holes to determine the orientation of the pair, and the known distance between the holes to determine the microscope magnification. However, we found that it is simpler to use a single hole and move the microscope or the calibration wafer with the AMTI robot in order to determine both the magnification and the orientation of the microscopes with respect to either robot or world coordinates.

The process of calibrating the two microscope cameras is as follows:

1. The calibration wafer is first placed in the center location of the pallet. The downward looking microscope views the pin in the calibration wafer from three non-collinear positions by translating the robot in the *x* and *y* directions. The microscope magnification and orientation are determined from the image position of the pin and the measured robot positions.

2. The wafer is carefully picked up and brought over to the upward looking microscope. Again, the robot is translated to three non-collinear positions, and the upward looking microscope views the same pin from the bottom side of the wafer. The microscope magnification and orientation are determined for the upward looking microscope.

3. The wafer is next rotated and translated to several positions within the field of view of the upward looking microscope. From the image positions of the pin and the measured robot positions, the position of the upward looking microscope in world coordinates and the position offset of the pin with respect to the robot tool coordinates are computed.

4. Once the position offset of the pin is known, the position of the downward looking microscope with respect to the robot tool coordinates is computed. This assumes that the wafer did not shift in the *x* or *y* directions when the robot picked it up.

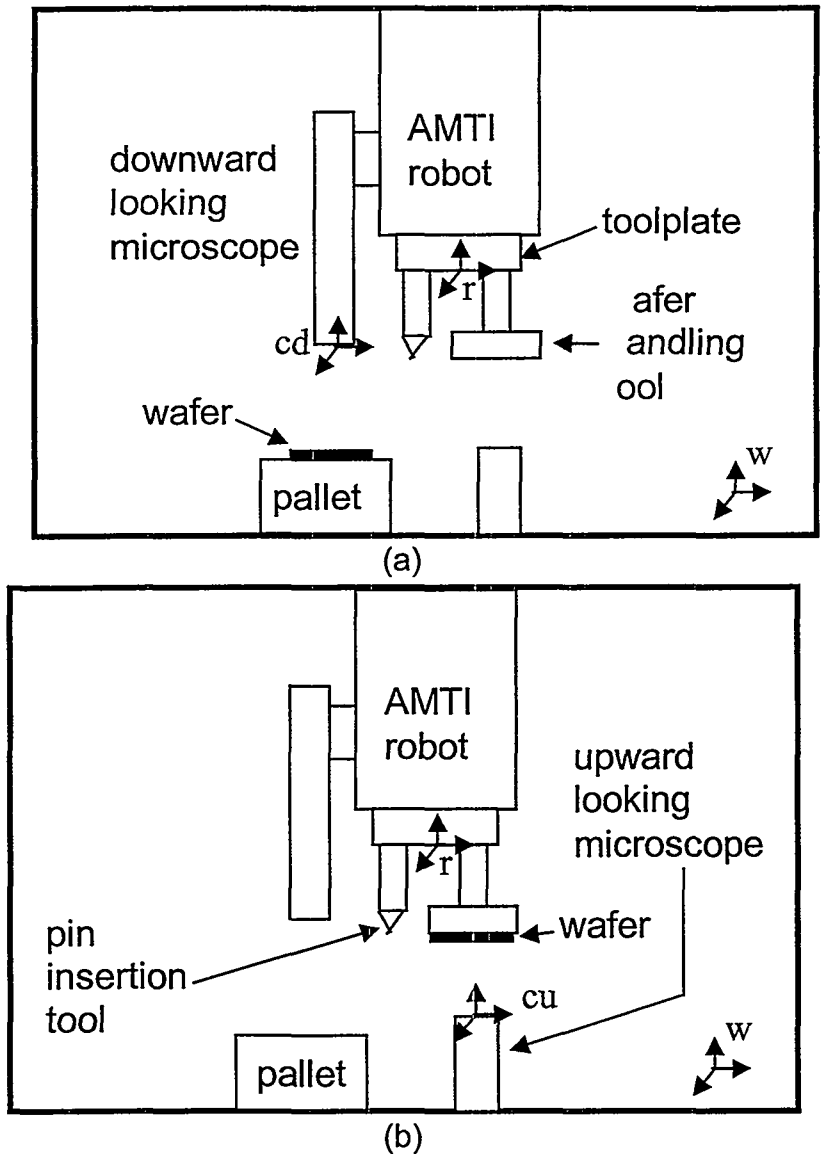


*Figure 6.4 (a) Calibration wafer being viewed by the downward looking microscope. (b) Calibration wafer being viewed by the upward looking microscope.*

Figure 6.4 illustrates a schematic of the workcell and the coordinate frames that describe the position and orientation of the various components. Homogeneous transformations are used to describe the relative positions and orientations between components. The transformations are:

${}^{w}\mathbf{T}_{r}$ = Position and orientation of the robot tool plate with respect to the world;

${}^{w}\mathbf{T}_{rxyz}$ = Position (excluding orientation) of the robot tool plate with respect to the world;

${}^{rxyz}\mathbf{T}_{cd}$ = Position and orientation of the downward looking microscope camera with respect to the robot position;

${}^{w}\mathbf{T}_{cu}$ = Position and orientation of upward looking microscope camera with respect to the world.

When the downward looking microscope is viewing the calibration wafer in the pallet, the position of a feature *f* (the calibration pin) with respect to the downward camera is related to the same position with respect to the world by

$$ {}^{w}\mathbf{p}_{f} = {}^{w}\mathbf{T}_{rxyz}\,{}^{rxyz}\mathbf{T}_{cd}\,{}^{cd}\mathbf{p}_{f} \quad . \tag{6.1} $$

where ${}^{w}\mathbf{p}_{f}$ is the position of feature *f* with respect to the world, and ${}^{cd}\mathbf{p}_{f}$ is the position of feature *f* with respect to downward looking camera.

When the upward looking microscope is viewing the calibration wafer while the robot is holding it, the position of the feature with respect to the upward looking camera is related to the same position with respect to the robot by

$$ {}^{w}\mathbf{T}_{r}\,{}^{r}\mathbf{p}_{f} = {}^{w}\mathbf{T}_{cu}\,{}^{cu}\mathbf{p}_{f} \quad . \tag{6.2} $$

where ${}^{r}\mathbf{p}_{f}$ is the position and orientation of feature *f* with respect to the robot tool plate, and ${}^{cu}\mathbf{p}_{f}$ is the position of feature *f* with respect to the upward looking camera.

In addition, the following transformations map 3-D positions into 2-D image coordinates:

$$ {}^{Icd}\mathbf{p}_{f} = \mathbf{S}_{cd}\,{}^{cd}\mathbf{p}_{f} \tag{6.3} $$

$$ {}^{Icu}\mathbf{p}_{f} = \mathbf{S}_{cu}\,{}^{cu}\mathbf{p}_{f} \tag{6.4} $$

where ${}^{Icd}\mathbf{p}_{f}$ and ${}^{Icu}\mathbf{p}_{f}$ are the positions of the feature in image coordinates, and $\mathbf{S}_{cd}$ and $\mathbf{S}_{cu}$ are the perspective transformations of the downward and upward looking cameras.

In these equations, ${}^{w}\mathbf{T}_{rxyz}$ and ${}^{w}\mathbf{T}_{r}$ are the measured positions of the robot, and ${}^{Icd}\mathbf{p}_{f}$ and ${}^{Icu}\mathbf{p}_{f}$ are the measured positions of the feature from the downward and upward looking microscopes. The objective of the calibration process is to find the transformations ${}^{rxyz}\mathbf{T}_{cd}$, ${}^{w}\mathbf{T}_{cu}$, $\mathbf{S}_{cd}$, and $\mathbf{S}_{cu}$.

These transformations can be simplified from the normal 6-dimensional representation to a 3-dimensional representation if the following assumptions hold:

A1. Since the AMTI robot is a 4 degree-of-freedom system, all assembly operations are constrained to (*x,y,z*) translation and rotation about the *z* axis.

A2. Within the field of view of the downward and upward looking microscopes, the short depth of field constrains the *z* dimension to be a constant.

Therefore, within the field of view of the microscopes, the transformations are constrained to *x* and *y* translation and rotation about the *z*-axis.

First, let us consider step 1 of the calibration process. The downward looking microscope camera, *cd*, is rigidly attached to the *x,y,z* translation stage of the AMTI robot. Orienting the fourth axis does not effect the position of the downward looking microscope. The position of the hole on the wafer with respect to the world coordinates $({}^{w}x, {}^{w}y)$ is related to the same position with respect to the camera $({}^{cd}x, {}^{cd}y)$ by

$$\begin{bmatrix} {}^{w}x \\ {}^{w}y \\ 1 \end{bmatrix} = \begin{bmatrix} 1 & 0 & {}^{w}x_r \\ 0 & 1 & {}^{w}y_r \\ 0 & 0 & 1 \end{bmatrix} \begin{bmatrix} \cos\alpha & -\sin\alpha & {}^{rxyz}x_{cd} \\ \sin\alpha & \cos\alpha & {}^{rxyz}y_{cd} \\ 0 & 0 & 1 \end{bmatrix} \begin{bmatrix} {}^{cd}x \\ {}^{cd}y \\ 1 \end{bmatrix} \tag{6.5}$$

where $({}^{w}x_r, {}^{w}y_r)$ is the position of the robot tool with respect to the world coordinates, $({}^{rxyz}x_{cd}, {}^{rxyz}y_{cd})$ is the position of the downward looking camera with respect to the robot tool (without orientation about *z*), and $\alpha$ is the orientation of the camera about *z* with respect to the robot tool (without orientation about *z*).

The microscope scales the position of the hole with respect to the downward looking camera by

$$\begin{bmatrix} {}^{Icd}x \\ {}^{Icd}y \\ 1 \end{bmatrix} = \begin{bmatrix} m_{xcd} & 0 & 0 \\ 0 & m_{ycd} & 0 \\ 0 & 0 & 1 \end{bmatrix} \begin{bmatrix} {}^{cd}x \\ {}^{cd}y \\ 1 \end{bmatrix} \tag{6.6}$$

where $({}^{Icd}x, {}^{Icd}y)$ is the position of the hole in pixels, and $(m_{xcd}, m_{ycd})$ are the *x,y* microscope magnification factors.

Combining Equations (6.5) and (6.6),

$$\begin{bmatrix} {}^{Icd}x \\ {}^{Icd}y \end{bmatrix} = \begin{bmatrix} m_{xcd} & 0 \\ 0 & m_{ycd} \end{bmatrix} \begin{bmatrix} \cos\alpha & \sin\alpha \\ -\sin\alpha & \cos\alpha \end{bmatrix} \left\{ \begin{bmatrix} {}^{w}x \\ {}^{w}y \end{bmatrix} - \begin{bmatrix} {}^{w}x_r \\ {}^{w}y_r \end{bmatrix} - \begin{bmatrix} {}^{rxyz}x_{cd} \\ {}^{rxyz}y_{cd} \end{bmatrix} \right\} \tag{6.7}$$

Since the x,y positioning repeatability of the AMTI robot is 0.4 microns, we assume that the robot's position is exact and is known. Also, we are able to measure the position of the hole in image coordinates ($^{Icd}x$, $^{Icd}y$). However, the microscope magnification ($m_{xcd}, m_{ycd}$), the position and orientation of the camera with respect to the robot tool ($^{rxyz}x_{cd}$, $^{rxyz}y_{cd}, \alpha$), and the position of the hole with respect to the world coordinates ($^{w}x$, $^{w}y$) are not known.

By moving the robot and downward looking camera to three non-collinear positions and recording the location of the hole in image coordinates, we can determine the microscope magnification and orientation of the camera. Since ($^{rxyz}x_{cd}$, $^{rxyz}y_{cd}$) and ($^{w}x$, $^{w}y$) are constant,

$$\begin{bmatrix} (^{Icd}x_2 - ^{Icd}x_1) & (^{Icd}x_3 - ^{Icd}x_2) \\ (^{Icd}y_2 - ^{Icd}y_1) & (^{Icd}y_3 - ^{Icd}y_2) \end{bmatrix} = \begin{bmatrix} m_{xcd}\cos\alpha & m_{ycd}\sin\alpha \\ -m_{ycd}\sin\alpha & m_{xcd}\cos\alpha \end{bmatrix} \begin{bmatrix} (^{w}x_{r2} - ^{w}x_{r1}) & (^{w}x_{r3} - ^{w}x_{r2}) \\ (^{w}y_{r2} - ^{w}y_{r1}) & (^{w}y_{r3} - ^{w}y_{r2}) \end{bmatrix}. \quad (6.8)$$

In general,

$$\begin{bmatrix} m_{xcd}\cos\alpha & m_{ycd}\sin\alpha \\ -m_{ycd}\sin\alpha & m_{xcd}\cos\alpha \end{bmatrix} = \begin{bmatrix} (^{Icd}x_2 - ^{Icd}x_1) & (^{Icd}x_3 - ^{Icd}x_2) \\ (^{Icd}y_2 - ^{Icd}y_1) & (^{Icd}y_3 - ^{Icd}y_2) \end{bmatrix} \begin{bmatrix} (^{w}x_{r2} - ^{w}x_{r1}) & (^{w}x_{r3} - ^{w}x_{r2}) \\ (^{w}y_{r2} - ^{w}y_{r1}) & (^{w}y_{r3} - ^{w}y_{r2}) \end{bmatrix}^{-1}. \quad (6.9)$$

Solving for the three unknowns is simplified if the robot moves only in the *x* direction between points 1 and 2 and then moves only in the *y* direction between points 2 and 3, i.e. $(^{w}y_{r2} - ^{w}y_{r1}) = 0$ and $(^{w}x_{r3} - ^{w}x_{r2}) = 0$. Solving for the angle of the camera and the *x,y* microscope magnification

$$\alpha = \arctan\left( \frac{\left(^{Icd}y_1 - ^{Icd}y_2\right) \Big/ \left(^{w}x_{r2} - ^{w}x_{r1}\right)}{\left(^{Icd}y_3 - ^{Icd}y_2\right) \Big/ \left(^{w}y_{r3} - ^{w}y_{r2}\right)} \right), \quad (6.10)$$

$$m_{xcd} = \frac{\left(^{Icd}x_3 - ^{Icd}x_2\right)}{\left(^{w}y_{r3} - ^{w}y_{r2}\right)\sin\alpha} \quad \text{and} \quad m_{ycd} = \frac{-\left(^{Icd}y_2 - ^{Icd}y_1\right)}{\left(^{w}x_{r2} - ^{w}x_{r1}\right)\sin\alpha} \quad \text{if} \quad |\sin\alpha| > 0.01, \quad (6.11)$$

$$\text{or} \quad m_{xcd} = \frac{\left(^{Icd}x_2 - ^{Icd}x_1\right)}{\left(^{w}x_{r2} - ^{w}x_{r1}\right)\cos\alpha} \quad \text{and} \quad m_{ycd} = \frac{\left(^{Icd}y_3 - ^{Icd}y_2\right)}{\left(^{w}y_{r3} - ^{w}y_{r2}\right)\cos\alpha} \quad \text{if} \quad |\sin\alpha| < 0.01. \quad (6.12)$$

If image noise is a problem, then the robot should be moved to more than 3 points, and a least squares approach [58] should be used to solve for Equation (6.8). As will be shown in the Experimental Results Section, image noise was not a problem, so a unique solution was adequate.

Similarly, we can solve for the microscope magnification and orientation of the upward looking microscope (step 2 of the calibration process). In this case, the

robot picks up the calibration wafer and the upward looking microscope views the pin from the underside of the wafer. The position of the hole on the wafer with respect to the robot tool $({}^{r}x, {}^{r}y)$ is related to the same position with respect to the upward looking camera $({}^{cu}x, {}^{cu}y)$ by

$$\begin{bmatrix} 1 & 0 & {}^{w}x_{r} \\ 0 & 1 & {}^{w}y_{r} \\ 0 & 0 & 1 \end{bmatrix} \begin{bmatrix} {}^{r}x \\ {}^{r}y \\ 1 \end{bmatrix} = \begin{bmatrix} \cos\beta & -\sin\beta & {}^{w}x_{cu} \\ \sin\beta & \cos\beta & {}^{w}y_{cu} \\ 0 & 0 & 1 \end{bmatrix} \begin{bmatrix} {}^{cu}x \\ {}^{cu}y \\ 1 \end{bmatrix} \tag{6.13}$$

where $({}^{w}x_{r}, {}^{w}y_{r})$ is the position of the robot tool (without orientation about z) with respect to the world coordinates, $({}^{w}x_{cu}, {}^{w}y_{cu})$ is the position of the upward looking camera with respect to the world coordinates, and $\beta$ is the orientation of the camera about z with respect to the world coordinates. For now, the orientation of the robot tool is assumed to be zero.

The microscope scales the position of the hole with respect to the upward looking camera by

$$\begin{bmatrix} {}^{Icu}x \\ {}^{Icu}y \\ 1 \end{bmatrix} = \begin{bmatrix} m_{xcu} & 0 & 0 \\ 0 & m_{ycu} & 0 \\ 0 & 0 & 1 \end{bmatrix} \begin{bmatrix} {}^{cu}x \\ {}^{cu}y \\ 1 \end{bmatrix} \tag{6.14}$$

where $({}^{Icu}x, {}^{Icu}y)$ is the position of the hole in pixels, and $(m_{xcu}, m_{ycu})$ are the x,y microscope magnification factors.

Combining Equations (6.13) and (6.14),

$$\begin{bmatrix} {}^{Icu}x \\ {}^{Icu}y \end{bmatrix} = \begin{bmatrix} m_{xcu} & 0 \\ 0 & m_{ycu} \end{bmatrix} \begin{bmatrix} \cos\beta & \sin\beta \\ -\sin\beta & \cos\beta \end{bmatrix} \left\{ \begin{bmatrix} {}^{w}x_{r} \\ {}^{w}y_{r} \end{bmatrix} + \begin{bmatrix} {}^{r}x \\ {}^{r}y \end{bmatrix} - \begin{bmatrix} {}^{w}x_{cu} \\ {}^{w}y_{cu} \end{bmatrix} \right\}. \tag{6.15}$$

The position of the hole in image coordinates $({}^{Icu}x, {}^{Icu}y)$ and the robot position $({}^{w}x_{r}, {}^{w}y_{r})$ can be measured. However, the microscope magnification $(m_{xcu}, m_{ycu})$, the position and orientation of the camera with respect to the world $({}^{w}x_{cu}, {}^{w}y_{cu}, \beta)$, and the position of the hole with respect to the robot tool $({}^{r}x, {}^{r}y)$ are not known.

By moving the robot and the calibration wafer to three non-collinear positions and recording the location of the hole in image coordinates, the microscope magnification and orientation of the camera can be determined. Since $({}^{r}x, {}^{r}y)$ and $({}^{w}x_{cu}, {}^{w}y_{cu})$ are constant,

$$\begin{bmatrix} ({}^{Icu}x_2 - {}^{Icu}x_1) & ({}^{Icu}x_3 - {}^{Icu}x_2) \\ ({}^{Icu}y_2 - {}^{Icu}y_1) & ({}^{Icu}y_3 - {}^{Icu}y_2) \end{bmatrix} = \begin{bmatrix} m_{xcu}\cos\beta & m_{ycu}\sin\beta \\ -m_{ycu}\sin\beta & m_{xcu}\cos\beta \end{bmatrix} \begin{bmatrix} ({}^{w}x_{r2} - {}^{w}x_{r1}) & ({}^{w}x_{r3} - {}^{w}x_{r2}) \\ ({}^{w}y_{r2} - {}^{w}y_{r1}) & ({}^{w}y_{r3} - {}^{w}y_{r2}) \end{bmatrix}. \quad (6.16)$$

In general,

$$\begin{bmatrix} m_{xcu}\cos\beta & m_{ycu}\sin\beta \\ -m_{ycu}\sin\beta & m_{xcu}\cos\beta \end{bmatrix} = \begin{bmatrix} ({}^{Icu}x_2 - {}^{Icu}x_1) & ({}^{Icu}x_3 - {}^{Icu}x_2) \\ ({}^{Icu}y_2 - {}^{Icu}y_1) & ({}^{Icu}y_3 - {}^{Icu}y_2) \end{bmatrix} \begin{bmatrix} ({}^{w}x_{r2} - {}^{w}x_{r1}) & ({}^{w}x_{r3} - {}^{w}x_{r2}) \\ ({}^{w}y_{r2} - {}^{w}y_{r1}) & ({}^{w}y_{r3} - {}^{w}y_{r2}) \end{bmatrix}^{-1}. \quad (6.17)$$

Solving for the three unknowns is simplified if the robot moves only in the x direction between points 1 and 2 and then moves only in the y direction between points 2 and 3, i.e. $({}^{w}y_{r2} - {}^{w}y_{r1}) = 0$ and $({}^{w}x_{r3} - {}^{w}x_{r2}) = 0$. Solving for the angle of the camera and the *x,y* microscope magnification

$$\beta = \arctan\left( \frac{\left({}^{Icu}y_1 - {}^{Icu}y_2\right) \Big/ \left({}^{w}x_{r2} - {}^{w}x_{r1}\right)}{\left({}^{Icu}y_3 - {}^{Icu}y_2\right) \Big/ \left({}^{w}y_{r3} - {}^{w}y_{r2}\right)} \right), \quad (6.18)$$

$$m_{xcu} = \frac{\left({}^{Icu}x_3 - {}^{Icu}x_2\right)}{\left({}^{w}y_{r3} - {}^{w}y_{r2}\right)\sin\beta} \quad \text{and} \quad m_{ycu} = \frac{-\left({}^{Icu}y_2 - {}^{Icu}y_1\right)}{\left({}^{w}x_{r2} - {}^{w}x_{r1}\right)\sin\beta} \quad \text{if} \quad |\sin\beta| > 0.01, \quad (6.19)$$

$$\text{or} \quad m_{xcu} = \frac{\left({}^{Icu}x_2 - {}^{Icu}x_1\right)}{\left({}^{w}x_{r2} - {}^{w}x_{r1}\right)\cos\beta} \quad \text{and} \quad m_{ycu} = \frac{\left({}^{Icu}y_3 - {}^{Icu}y_2\right)}{\left({}^{w}y_{r3} - {}^{w}y_{r2}\right)\cos\beta} \quad \text{if} \quad |\sin\beta| < 0.01. \quad (6.20)$$

Now that the magnification and orientation of each microscope are known, we can go back and determine the position of each microscope (step 3 of the calibration process). For the upward looking microscope, we are interested in its position with respect to the world coordinates. For the downward looking microscope, we are interested in its position with respect to the robot's tool frame.

Let us begin with the upward looking microscope. To determine its position with respect to the world, we need to find the position of the hole in the calibration wafer with respect to the robot's tool coordinates. This can be accomplished by viewing the hole while rotating the robot's wrist. The set of equations that describe the position of the hole are

$$\begin{bmatrix} \cos\theta & -\sin\theta & {}^{w}x_r \\ \sin\theta & \cos\theta & {}^{w}y_r \\ 0 & 0 & 1 \end{bmatrix} \begin{bmatrix} {}^{r}x \\ {}^{r}y \\ 1 \end{bmatrix} = \begin{bmatrix} \cos\beta & -\sin\beta & {}^{w}x_{cu} \\ \sin\beta & \cos\beta & {}^{w}y_{cu} \\ 0 & 0 & 1 \end{bmatrix} \begin{bmatrix} 1/m_{xcu} & 0 & 0 \\ 0 & 1/m_{ycu} & 0 \\ 0 & 0 & 1 \end{bmatrix} \begin{bmatrix} {}^{Icu}x \\ {}^{Icu}y \\ 1 \end{bmatrix} \quad (6.21)$$

where $\theta$ is the orientation of the robot wrist about the *z*-axis. From above, we know $(m_{xcu}, m_{ycu}, \beta)$. We can measure the robot position and orientation $({}^{w}x_r, {}^{w}y_r, \theta)$ and the position of the hole in the image plane $({}^{Icu}x, {}^{Icu}y)$. However, we do not know the position of the hole relative to the robot tool frame $({}^{r}x, {}^{r}y)$ or the position of the microscope with respect to the world coordinates $({}^{w}x_{cu}, {}^{w}y_{cu})$. There are two equations and four unknowns. Equation (21) can be written as

$$f_i = \begin{bmatrix} \cos\theta & -\sin\theta & -1 & 0 \\ \sin\theta & \cos\theta & 0 & -1 \end{bmatrix} \begin{bmatrix} {}^{r}x \\ {}^{r}y \\ {}^{w}x_{cu} \\ {}^{w}y_{cu} \end{bmatrix} - \begin{bmatrix} X_i \\ Y_i \end{bmatrix} = 0 \tag{6.22}$$

where

$$\begin{bmatrix} X_i \\ Y_i \end{bmatrix} = \begin{bmatrix} -{}^{w}x_{ri} + \dfrac{{}^{Icu}x_i}{m_{xcu}}\cos\beta - \dfrac{{}^{Icu}y_i}{m_{ycu}}\sin\beta \\ -{}^{w}y_{ri} + \dfrac{{}^{Icu}x_i}{m_{xcu}}\sin\beta + \dfrac{{}^{Icu}y_i}{m_{ycu}}\cos\beta \end{bmatrix} \tag{6.23}$$

Moving the hole to $n>2$ points, the least squares problem can be stated as

$$\min_{\Theta} \sum_{i=1}^{n} f_i^T f_i = \min_{\Theta} (A\Theta - b)^T (A\Theta - b) \tag{6.24}$$

where

$$A = \begin{bmatrix} \cos\theta_1 & -\sin\theta_1 & -1 & 0 \\ \sin\theta_1 & \cos\theta_1 & 0 & -1 \\ \vdots & \vdots & \vdots & \vdots \\ \cos\theta_n & -\sin\theta_n & -1 & 0 \\ \sin\theta_n & \cos\theta_n & 0 & -1 \end{bmatrix}, \quad b = \begin{bmatrix} X_1 \\ Y_1 \\ \vdots \\ X_n \\ Y_n \end{bmatrix}, \quad \text{and} \quad \Theta = \begin{bmatrix} {}^{r}x \\ {}^{r}y \\ {}^{w}x_{cu} \\ {}^{w}y_{cu} \end{bmatrix}.$$

The well-known least squares solution is

$$\Theta = (A^T A)^{-1} A^T b. \tag{6.25}$$

If the robot angle $\theta_i$ is not known precisely, an alternative method of locating the position of the upward looking microscope is as follows. First, locate the center of the robot tool in the upward looking camera coordinates, and then add the position of the robot tool with respect to world coordinates. By rotating the robot tool, the

hole in the calibration wafer creates an arc in the image coordinates whose center is the robot tool position in camera coordinates. The least squares problem is to

$$\min_{\left({}^{cu}x_r, {}^{cu}y_r, {}^{cu}r\right)} \sum_{i=1}^{n}\left[\left({}^{cu}x_i - {}^{cu}x_r\right)^2 + \left({}^{cu}y_i - {}^{cu}y_r\right)^2 - \left({}^{cu}r\right)^2\right]^2 \tag{6.26}$$

where

$$\begin{bmatrix} {}^{cu}x_i \\ {}^{cu}y_i \\ 1 \end{bmatrix} = \begin{bmatrix} \cos\beta & -\sin\beta & 0 \\ \sin\beta & \cos\beta & 0 \\ 0 & 0 & 1 \end{bmatrix} \begin{bmatrix} 1/m_{xcu} & 0 & 0 \\ 0 & 1/m_{ycu} & 0 \\ 0 & 0 & 1 \end{bmatrix} \begin{bmatrix} {}^{Icu}x_i \\ {}^{Icu}y_i \\ 1 \end{bmatrix}.$$

The location of the upward looking microscope in world coordinates is then

$$\begin{bmatrix} {}^{w}x_{cu} \\ {}^{w}y_{cu} \\ 1 \end{bmatrix} = \begin{bmatrix} {}^{w}x_r \\ {}^{w}y_r \\ 1 \end{bmatrix} - \begin{bmatrix} {}^{cu}x_r \\ {}^{cu}y_r \\ 1 \end{bmatrix} \tag{6.27}$$

where $({}^{cu}x_r, {}^{cu}y_r)$ is the solution to (6.26).

The location of the downward looking microscope with respect to the robot coordinate frame is the last unknown (step 4 of the calibration process). Unfortunately, we can not use the same technique as above. Instead, we must assume that the robot gently picked up the wafer without moving it laterally. As we will see in the Experimental Results Section, this is a good assumption. The absolute position of the hole $({}^{w}x_{hp}, {}^{w}y_{hp})$ when the wafer is on the pallet is

$$\begin{bmatrix} {}^{w}x_{hp} \\ {}^{w}y_{hp} \\ 1 \end{bmatrix} = \begin{bmatrix} \cos\theta_p & -\sin\theta_p & {}^{w}x_{rp} \\ \sin\theta_p & \cos\theta_p & {}^{w}y_{rp} \\ 0 & 0 & 1 \end{bmatrix} \begin{bmatrix} {}^{r}x \\ {}^{r}y \\ 1 \end{bmatrix} \tag{6.28}$$

where $({}^{r}x, {}^{r}y)$ is the relative position of the hole with respect to the robot wrist as found in Equation (6.25), and $({}^{w}x_{rp}, {}^{w}y_{rp}, \theta_p)$ are the position and orientation of the robot when the wafer is picked up from the pallet. The position of the downward looking microscope $({}^{rxyz}x_{cd}, {}^{rxyz}y_{cd})$ can be computed as

$$\begin{bmatrix} {}^{rxyz}x_{cd} \\ {}^{rxyz}y_{cd} \\ 1 \end{bmatrix} = \begin{bmatrix} {}^{w}x_{hp} \\ {}^{w}y_{hp} \\ 1 \end{bmatrix} - \begin{bmatrix} 1 & 0 & {}^{w}x_{ri} \\ 0 & 1 & {}^{w}y_{ri} \\ 0 & 0 & 1 \end{bmatrix} \begin{bmatrix} \cos\gamma & -\sin\gamma & 0 \\ \sin\gamma & \cos\gamma & 0 \\ 0 & 0 & 1 \end{bmatrix} \begin{bmatrix} 1/m_{xcd} & 0 & 0 \\ 0 & 1/m_{ycd} & 0 \\ 0 & 0 & 1 \end{bmatrix} \begin{bmatrix} {}^{Icd}x_i \\ {}^{Icd}y_i \\ 1 \end{bmatrix} \quad (6.29)$$

where $({}^{w}x_{ri}, {}^{w}y_{ri})$ is anyone of the three positions (*i=1,2,or 3*) of the robot when viewing the hole with the downward looking microscope (see Equations (6.10) to (6.12)), and $({}^{Icd}x_i, {}^{Icd}y_i)$ is the corresponding position of the hole in the image.

Once calibrated, the vision system can be used to determine the position of pins and gears and the tool offset of the pin insertion tool. For example, the location of a pin or hole $({}^{w}x_{fd}, {}^{w}y_{fd})$ can be determined from the image coordinates of the downward looking microscope by

$$\begin{bmatrix} {}^{w}x_{fd} \\ {}^{w}y_{fd} \\ 1 \end{bmatrix} = \begin{bmatrix} 1 & 0 & {}^{w}x_{rfd} \\ 0 & 1 & {}^{w}y_{rfd} \\ 0 & 0 & 1 \end{bmatrix} \begin{bmatrix} \cos\gamma & -\sin\gamma & {}^{rxyz}x_{cd} \\ \sin\gamma & \cos\gamma & {}^{rxyz}y_{cd} \\ 0 & 0 & 1 \end{bmatrix} \begin{bmatrix} 1/m_{xcd} & 0 & 0 \\ 0 & 1/m_{ycd} & 0 \\ 0 & 0 & 1 \end{bmatrix} \begin{bmatrix} {}^{Icd}x_{fd} \\ {}^{Icd}y_{fd} \\ 1 \end{bmatrix} \quad (6.30)$$

where $({}^{Icd}x_{fd}, {}^{Icd}y_{fd})$ is the image position of the feature, and $({}^{w}x_{rfd}, {}^{w}y_{rfd})$ is the position of the robot when the image is taken.

Using the upward looking microscope, the position offset of the pin insertion tool is determined from a hole in the center of the tool. Its position offset with respect to the robot wrist $({}^{r}x_{fu}, {}^{r}y_{fu})$ is given by

$$\begin{bmatrix} {}^{r}x_{fu} \\ {}^{r}y_{fu} \\ 1 \end{bmatrix} = \begin{bmatrix} \cos\theta_{fu} & -\sin\theta_{fu} & {}^{w}x_{r} \\ \sin\theta_{fu} & \cos\theta_{fu} & {}^{w}y_{r} \\ 0 & 0 & 1 \end{bmatrix}^{-1} \begin{bmatrix} \cos\beta & -\sin\beta & {}^{w}x_{cu} \\ \sin\beta & \cos\beta & {}^{w}y_{cu} \\ 0 & 0 & 1 \end{bmatrix} \begin{bmatrix} 1/m_{xcu} & 0 & 0 \\ 0 & 1/m_{ycu} & 0 \\ 0 & 0 & 1 \end{bmatrix} \begin{bmatrix} {}^{Icu}x_{fu} \\ {}^{Icu}y_{fu} \\ 1 \end{bmatrix} \quad (6.31)$$

where $({}^{Icu}x_{fu}, {}^{Icu}y_{fu})$ is the image position of the insertion tool and $\theta_{fu}$ is the wrist orientation when the image is taken.

Using Equations (6.30) and (6.31), the pins can be picked up and inserted, and the gears and pins can be aligned. For example, when picking up a pin, the *x,y* position of the robot is determined by solving

$$\begin{bmatrix} {}^{w}x_{fd} \\ {}^{w}y_{fd} \\ 1 \end{bmatrix} = \begin{bmatrix} \cos\theta & -\sin\theta & {}^{w}x_{r} \\ \sin\theta & \cos\theta & {}^{w}y_{r} \\ 0 & 0 & 1 \end{bmatrix} \begin{bmatrix} {}^{r}x_{fu} \\ {}^{r}y_{fu} \\ 1 \end{bmatrix} \quad (6.32)$$

for $({}^{w}x_r, {}^{w}y_r)$ where $\theta$ is any arbitrary robot wrist angle, and $({}^{w}x_{fd}, {}^{w}y_{fd})$ and $({}^{r}x_{fu}, {}^{r}y_{fu})$ are the locations of the pin and pin insertion tool as given in Equations (30) and (31). When placing the wafer of gears on the press-fit pins, the *x,y* position and orientation of the robot are determined by solving

$$\begin{bmatrix} \cos\lambda & -\sin\lambda & {}^{w}x_{fd1} \\ \sin\lambda & \cos\lambda & {}^{w}y_{fd1} \\ 0 & 0 & 1 \end{bmatrix} = \begin{bmatrix} \cos\theta & -\sin\theta & {}^{w}x_r \\ \sin\theta & \cos\theta & {}^{w}y_r \\ 0 & 0 & 1 \end{bmatrix} \begin{bmatrix} \cos\gamma & -\sin\gamma & {}^{r}x_{fu1} \\ \sin\gamma & \cos\gamma & {}^{r}y_{fu1} \\ 0 & 0 & 1 \end{bmatrix} \tag{6.33}$$

for $({}^{w}x_r, {}^{w}y_r, \theta)$. The locations of pins 1 and 2 with respect to the world coordinates are $({}^{w}x_{fd1}, {}^{w}y_{fd1})$ and $({}^{w}x_{fd2}, {}^{w}y_{fd2})$ as given in Equation (6.30). The locations of gears 1 and 2 with respect to the robot coordinates are $({}^{r}x_{fu1}, {}^{r}y_{fu1})$ and $({}^{r}x_{fu2}, {}^{r}y_{fu2})$ as given in Equation (31). The orientations of the pins and gears are given by

$$\lambda = \arctan\left(\frac{{}^{w}y_{fd2} - {}^{w}y_{fd1}}{{}^{w}x_{fd2} - {}^{w}x_{fd1}}\right) \quad \text{and} \quad \gamma = \arctan\left(\frac{{}^{r}y_{fu2} - {}^{r}y_{fu1}}{{}^{r}x_{fu2} - {}^{r}x_{fu1}}\right). \tag{6.34}$$

## 6.3 Experimental Results

The calibration procedure was executed several times to quantify the variability of the procedure. Tables 6.1 to 6.3 show the results of these tests. From Table 6.1, the resolution of the downward looking camera is approximately 5.9 microns/pixel, while the resolution of the upward looking camera is approximately 4.8 microns/pixel. However, when determining the center location of the holes, a subpixel precision of 3.3 microns (3 standard deviations -- 3σ) for the downward looking microscope and 1.3 microns (3σ) for the upward looking microscope was typically achieved.

Tables 6.2 and 6.3 show that the two methods for determining the upward looking microscope's location produce substantially different results. While the mean error in Table 6.2 is extremely low, the standard deviation (root mean squared error) shows that errors in the fit data can reach up to 68 microns (3σ). On the other hand, the standard deviation in Table 6.3 shows that errors in the fit data are typically less than 3.6 microns (3σ). These results lead us to conclude that the resolution of the wrist angle used in the calculations is not accurate enough. Although the wrist motor has a repeatability of 0.006 degrees, the belt between the motor and the wrist axis allows for considerable errors. In fact, we estimate the wrist errors to be up to 0.1 degrees over a 10 degree rotation, based on the circular fit using Equation (6.26). Therefore, the least squares fit using Equation (6.26) is used for calibration throughout the rest of the tests.

*Table 6.1. Vision calibration parameters for 10 trials.*

| | Mean (pixels/mm) | Standard Deviation |
|---|---|---|
| $m_{xcd}$ | 171.9016 pixels/mm | 0.18960 pixels/mm |
| $m_{ycd}$ | 173.4098 pixels/mm | 0.13797 pixels/mm |
| $\alpha$ | -88.5810 degrees | 0.01933 degrees |
| $m_{xcu}$ | -208.7504 pixels/mm | 0.09288 pixels/mm |
| $m_{ycu}$ | 209.3141 pixels/mm | 0.04987 pixels/mm |
| $\beta$ | -92.6970 degrees | 0.04705 pixels/mm |

*Table 6.2. Vision calibration parameters derived from fitting 9 data points using Equation (6.25).*

| | |
|---|---|
| ${}^{r}x$ | 20.6575 mm |
| ${}^{r}y$ | 22.9962 mm |
| Mean error from data point | $2.8816 \times 10^{-14}$ mm |
| Standard deviation from data point | 0.0227 mm |
| ${}^{w}x_{cu}$ | 125.0708 mm |
| ${}^{w}y_{cu}$ | 8.7608 mm |
| ${}^{rxyz}x_{cd}$ | 2.9427 mm |
| ${}^{rxyz}y_{cd}$ | 109.6385 mm |

*Table 6.3. Vision calibration parameters derived from fitting 9 data points using Equation (6.26). Matlab's LEASTSQ routine was used to solve the circular least squares fit.*

| | |
|---|---|
| ${}^{cu}x_{r}$ | 21.3728 mm |
| ${}^{cu}y_{r}$ | 24.8062 mm |
| ${}^{cu}r$ | 31.1236 mm |
| Mean error from circular fit | $-2.0 \times 10^{-8}$ mm |
| Standard deviation from circular fit | 0.0012 mm |
| ${}^{w}x_{cu}$ | 125.0496 mm |
| ${}^{w}y_{cu}$ | 8.5336 mm |
| ${}^{rxyz}x_{cd}$ | 2.9254 mm |
| ${}^{rxyz}y_{cd}$ | 109.4062 mm |

Because of possible errors in wrist orientation, we must also be careful when aligning rows of gears to rows of pins. Instead of applying Equations (6.33) and (6.34) only once, it is applied several times, allowing the visual feedback to correct for the wrist orientation error. In the future, we plan to add an additional encoder on the wrist axis to eliminate this orientation error.

To assess the accuracy of the calibration parameters in Table 6.1 and 6.3, another test was perform that compared the calculated location of the calibration pin before and after the robot picked up the wafer. First, the downward looking microscope viewed the calibration wafer while it was in the pallet, and the absolute position of the pin was computed. Next, the robot picked up the calibration wafer and translated it over the upward looking camera. The new absolute position of the calibration pin was computed from the upward looking microscope image coordinates. This position was compared to the translated position computed from the downward looking microscope. This test was repeated 10 times. Table 6.4 shows that the repeatability was 1.3 microns with a standard deviation of 0.5 microns. This error includes vision calibration errors as well as a possible displacement of the wafer when it is being picked up. Since the clearance holes of the gears are 8-11 microns larger than the pin diameters, these calibration results were concluded to be accurate enough to perform the gear placement task. If necessary, better resolution could be achieved by increasing the magnification of the microscopes, which are currently at their lowest setting.

*Table 6.4. Location errors of the calibration pin when viewed before and after the robot picked up the wafer.*

| | Mean | Standard Deviation |
|---|---|---|
| $e_x$ | 0.1040 microns | 0.3523 microns |
| $e_y$ | 1.2526 microns | 0.5365 microns |
| $\sqrt{e_x^2+e_y^2}$ | 1.3106 microns | 0.5088 microns |

Once the vision system is calibrated, the assembly process is as follows.

1. The upward looking microscope locates the center of the pin insertion tool with respect to the robot tool frame using Equation (6.31).
2. The downward looking microscope locates a pin in the left most wafer (the one with the clearance holes) using Equation (6.30).
3. The pin insertion tool is moved just above the pin using Equation (6.32). The downward pneumatic valve of the insertion tool is activated, pushing the tool over the pin. A vacuum is applied to the tool tip, picking up the pin. The upward value of the insertion tool is activated, lifting the tool.

4. The downward looking microscope locates a hole in the middle wafer (the one with press-fit holes) using Equation (6.30).
5. The pin insertion tool with the pin is moved just above the hole using Equation (6.32). The downward valve of the insertion tool is activated, pressing the pin into the hole. The vacuum at the tool tip is released, and the upward valve of the insertion tool is activated, thus lifting the tool and leaving the press-fit pin.
6. Steps 2 through 5 are repeated for several pins.
7. The downward looking microscope locates two pins in the middle wafer using Equation (6.30). The orientation of the rows of pins is determined from these two positions from Equation (6.34).
8. The vacuum chuck tool picks up the right wafer (the one with the gears) and positions it over the upward looking microscope.
9. The upward looking microscope locates the center of two gears with respect to the robot tool frame using Equation (6.31). The orientation of the rows of gears is determined from these two positions from Equation (6.34). The robot wrist is rotated to align the orientation of the rows of gears to the rows of pins. Because of possible wrist rotation error, this step is repeated several times until an acceptable error is reached.
10. The robot places the wafer of gears over the wafer of pins using Equation (6.33).

Figure 6.5 shows the robot picking up a 386-micron diameter pin. Figures 6.6 and 6.7 show the robot placing the wafer of gears over the wafer of pins. These experiments were repeated several times, and as long as the vision system correctly located a pin or hole, it never failed. In those cases where the vision system failed to locate a pin or hole, it was typically because of scratches or dust that had accumulated around the hole. At the time of publication, the gears have not been released from a top wafer. However, a close visual inspection from the side of the wafer shows that the gears are being placed on the pins. This is verified by the contact between the surface of the two wafers, and the fact that they do not slip laterally.

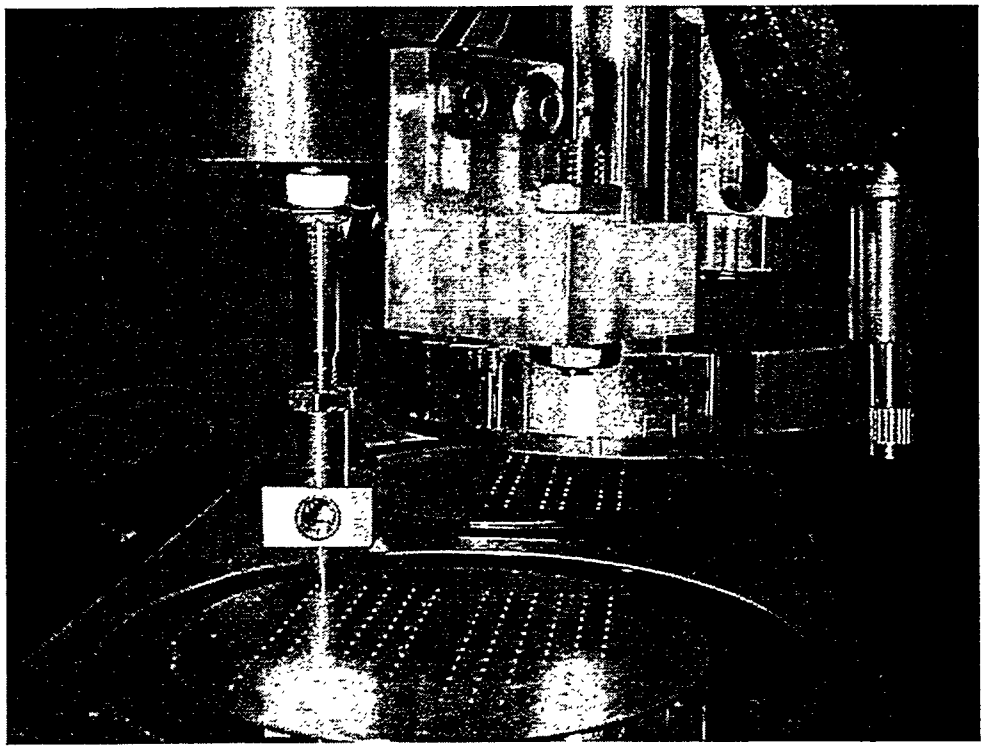

*Figure 6.5. The pin insertion tool is picking up a 386 micron diameter pin. The pin is placed in the wafer in the background.*

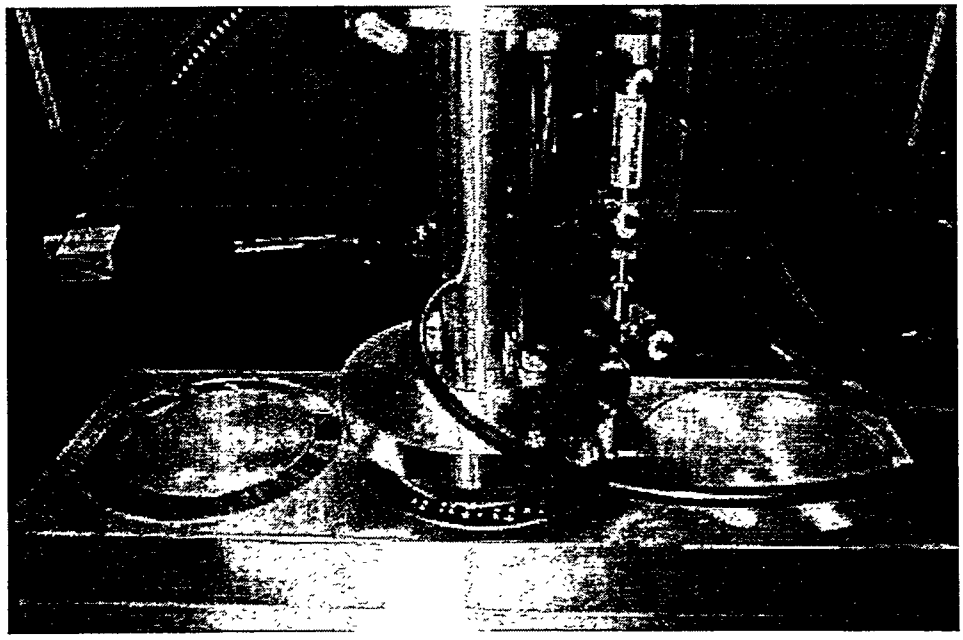

*Figure 6.6. The wafer of gears is being placed on the wafer of pins.*

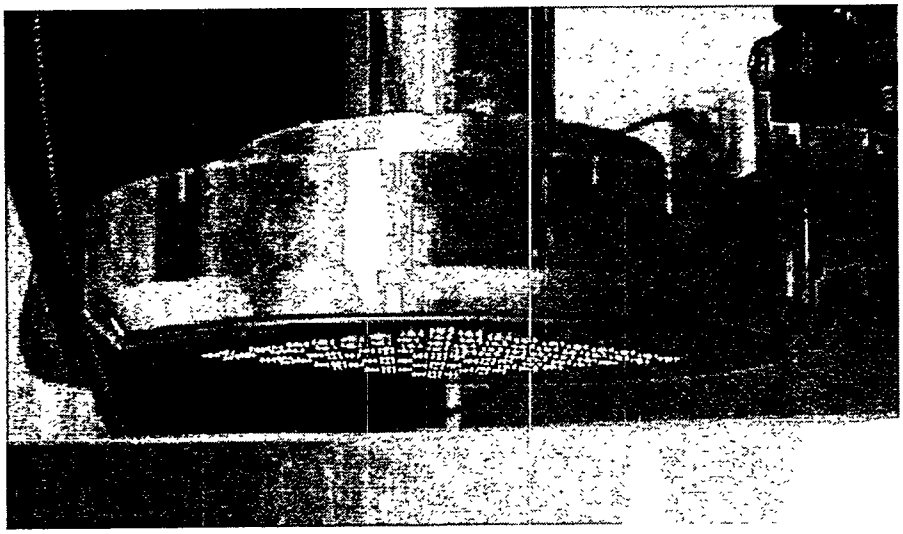

*Figure 6.7. View of the wafer of gears before being placed on the pins.*

## 7.0 Conclusions and Future Directions

In this report, we addressed several aspects of microassembly. In particular, we investigated the design and fabrication of micro-grippers, the use of visual feedback, microassembly planning, and parallel assembly techniques. Both theoretical and experimental work were performed. A prototype micromanipulation workcell was constructed to test many of the theoretical ideas.

Experimental tests in our workcell show that the LIGA tweezers are currently a better choice for manipulating the larger LIGA parts than the vacuum gripper or the polysilcon gripper. Even if the material of the vacuum gripper could be made nonmagnetic and the polysilicon tweezers were not as fragile, the LIGA tweezers have the following advantages. First, by picking up the part from the side, the tweezers allow a machine vision system to view the parts from above and make fine adjustments to their position. Second, strain gages can be fabricated onto the tweezers, thus allowing the grasping force to be monitored and controlled. Third, the collet arrangement allows the robotic system to change tweezer geometries for the particular task at hand. However, there are still several areas which could be improved. First, material composition and coatings should be chosen to reduce sticking effects caused by surface tension, Van der Waals forces, electrostatics, and electromagnetics. Second, the DC linear motor is oversized for the task and contains some backlash in it's gearbox. In the future, it could be replaced by a more compact motor or a PZT actuator as in [9].

Within this project, we have also demonstrated the ability to visually servo the LIGA parts to a desired *x,y* position between the tweezers. Fourier optics methods were used to generate a synthetic image from a CAD model. This synthetic image was used to select image processing routines and generate reference features for visual servoing. Future research should concentrate on generating a sequence of synthetic images which represent assembly steps, e.g. tweezer grasps gear, locate shaft, and put gear on shaft. Again, these images will be used to select image processing routines and generate reference features for visual servoing.

We also took the first steps in explaining how to approach assembly planning in the micro-domain. We believe that free-space motion planning and the geometric assembly constraints in macro-world planners will directly apply to the micro-domain. However, fine motion planning and precise motion will differ from the macro-world. In particular, we have shown that van der Waals and electrostatic forces will alter the goal regions for pick-up, hold, and release tasks. In this report, we developed the mathematics necessary to locate these goal regions for a spherical part being manipulated by a rectangular block.

Since assembly planning in the micro-domain is a new area of research, much work still needs to be performed. Future work should concentrate on more complex part and tool shapes. Evaluation of van der Waals and electrostatic forces will become significantly more difficult as we investigate shapes other than spheres and rectangular blocks. Finite element models [40] will be required to compute the forces between these more complex shapes. Once the goal regions are specified,

realistic termination predicates using force, time, and vision as sensing modalities need to be specified. Instrumentation that can measure sub-micro-Newtons of force needs to be developed. Fine motion planning using visual constraints [59] that have been modified by diffraction effects at the micro-scale is also an area of research. Finally, how these goal regions affect planning under uncertainty needs to be addressed.

Lastly, we developed parallel assembly techniques for assembling multiple layers of LIGA parts into complex structures, such as a geared transmission. The "standard" processes for this parallel assembly would consist of four steps: fabrication, assembly, diffusion bonding, and release. These steps would be repeated several times, each time adding a new layer of LIGA to the final assembly. In this project, we investigated the assembly step. This step consists of automatically inserting multiple pins into a substrate, and then placing a wafer with multiple gears onto the pins. A dual microscope system was used to accurately locate the pins and align the wafers to within 3 microns. Future work should concentrate on integrating the assembly step with the diffusion bonding and release steps.

## References


1. R. Arai, D. Ando, T. Fukuda, Y. Nonoda, T. Oota, "Micro Manipulation Based on Micro Physics - Strategy Based on Attractive Force Reduction and Stress Measurement," *Proc. of ICRA 1995*, pp. 236-241.
2. R.S. Fearing, "Survey of Sticking Effects for Micro Parts Handling," *Proc. of IROS '95*, Pittsburgh, PA, August 1995, Vol. 2, pp. 212-217.
3. H. Miyazaki, T. Sato, "Pick and Place Shape Forming of Three-Dimensional Micro Structures from Fine Particles," *Proc. of ICRA 1996*, pp. 2535-2540.
4. K. Koyano, T. Sato, "Micro Object Handling System with Concentrated Visual Fields and New Handling Skills," *Proc. of ICRA 1996*, pp. 2541-2548.
5. M. Mitsuishi, N. Sugita, T. Nagao, Y. Hatamura, "A Tele-Micro Machining System with Operation Environment Transmission under a Stereo-SEM," *Proc. of ICRA 1996*, pp. 2194-2201.
6. A. Sulzmann, H.-M. Breguett, J. Jacot, "Microvision System (MVS): a 3D Computer Graphic-Based Microrobot Telemanipulation and Position Feedback by Vision," *Proc. of SPIE Vol. 2593*, Philadelphia, Oct. 25, 1995.
7. W. Zesch, M. Brunner, A. Weber, "Vacuum Tool for Handling Microobjects with a Nanorobot," *Proc. of ICRA 1997*, pp. 1761-1766.
8. C.G. Keller, R.T. Howe, "Hexsil Tweezers for Teleoperated Micro-Assembly," *Proc. MEMS97*, 1997.
9. S. Ballandras, S. Basrour, L. Robert, S. Megtert, P. Blind, M. Rouillay, P. Bernede, W. Daniau, "Microgrippers fabricated by the LIGA technique," Sensors and Actuators A 58 (1997) 265-272.
10. J.T. Feddema, C.G. Keller, R.T. Howe, "Experiments in Micromanipulation and CAD-Driven Microassembly," *Proc. of SPIE Vol. 3209*, pp. 98-107, Pittsburgh, Oct. 14-15, 1997.
11. J.T. Feddema, M. Polosky, T. Christenson, B. Spletzer, R. Simon, "Micro-Gripper for Assembly of LIGA Parts," *Proceedings of the World Automation Congress '98*, pp. ISORA-045.1 to 045.8, Anchorage, May 10-14, 1998.
12. J.T. Feddema, P. Xavier, R. Brown, "Assembly Planning at the Micro Scale," *Workshop on Precision Manipulation at the Micro and Nano Scales, 1998 IEEE International Conference on Robotics and Automation*, pp. 56-69, Leuven, Belgium, May 16-20, 1998.
13. J.T. Feddema, R. W. Simon, "CAD-Driven Microassembly and Visual Servoing," *Proceedings of the 1998 IEEE International Conference on Robotics and Automation*, Leuven, Belgium, May 16-20, 1998, pp. 1212-1219.
14. J.T. Feddema, R.W. Simon, "Visual Servoing and CAD Driven Microassembly," *IEEE Robotics and Automation Magazine*, pp. 18-24, December 1998.
15. J.T. Feddema, "Microassembly of Micro-Electro-Mechanical Systems (MEMS) using Visual Servoing," *The Confluence of Vision and Control*, ed. Kriegman, Hager, and Morse, Springer-Verlag London Limited, 1998.

16. J.T. Feddema, T. Christenson, "Parallel Assembly of LIGA Components," *Tutorial on Modeling and Control of Micro- and Nano-Manipulation, 1999 IEEE International Conference on Robotics and Automation*, Detroit, May 11, 1999.
17. C.G. Keller, "Microgrippers with Integrated Actuator and Force Sensors," *Proceedings of the World Automation Congress '98*, pp. ISORA-064.1 to 064.6, Anchorage, May 10-14, 1998.
18. P.I. Corke, ``Visual Control of Robot Manipulators - A Review," *Visual Servoing: Real-Time Control of Robot Manipulators Based on Visual Sensory Feedback*, Ed. K. Hashimoto, World Scientific Publishing Co. Pte. Ltd., Singapore, 1993.
19. S. Hutchinson, G.D. Hagar, P.I. Corke, "A Tutorial on Visual Servo Control," *IEEE Trans. On Robotics and Automation*, Vol. 12, No. 5, pp. 651-670, Oct. 1996.
20. A. Sulzmann, J. Jacot, "3D Computer Vision for Micro-assembly Station and Microfabrication," *Proc. of SPIE Vol. 3202,* Pittsburgh, Oct. 16, 1997.
21. B. Vikramaditya and B. J. Nelson, "Visually Guided Microassembly using Optical Microscope and Active Vision Techniques," *Proc. of ICRA 1997*, pp. 3172-3178.
22. A.P. Pentland, "A New Sense of Depth of Field," *IEEE Trans. on PAMI*, Vol. PAMI-9, No. 4, July 1987.
23. J. Ens and P. Lawrence, "An Investigation of Methods for Determining Depth of Focus," *IEEE Trans. on PAMI*, Vol. 15, No. 2, February 1993.
24. S.K. Nayar and Y. Nakagawa, "Shape from Focus," *IEEE Trans. on PAMI*, Vol. 16, No. 8, August 1994.
25. M. Subbarao and T.Choi, "Accurate Recovery of Three-Dimensional Shape from Image Focus," *IEEE Trans. on PAMI*, Vol. 17, No. 3, March 1995.
26. M. Bass, *Handbook of Optics*, 2nd Edition, Vol. II, pp. 17.1-17.52, McGraw-Hill, 1995.
27. L.C. Martin, *The Theory of the Microscope*, American Elsevier Publishing Company, 1966.
28. G.O. Reynolds, J.B. DeVelis, G.B. Parret, B.J. Thompson, *The New Physical Optics Notebook: Tutorials in Fourier Optics*, SPIE, 1989.
29. J.T. Feddema, C.S.G. Lee, and O.R. Mitchell, "Weighted Selection of Image Features for Resolved Rate Visual Feedback Control," *IEEE Trans. On Robotics and Automation*, Vol. 7, pp. 31-47, Feb. 1991.
30. J.-C. Latombe, *Robot Motion Planning*, 1991.
31. R. Allen Bowling, "A Theoretical Review of Particle Adhesion," *Particles on Surfaces 1*, K.L. Mittal, editor, pp. 129-142, 1988.
32. J.N Israelachvili, "The Nature of van der Waals Forces," *Contemporary Physics*, Vol. 15, No. 2, pp. 159-177, 1974.
33. H.C. Hamaker, "The London-van der Waals Attraction Between Spherical Particles," *Physica IV*, No. 10, pp. 1058-1072, November 1937.
34. E.M. Lifshitz, Sov. Phys. JETP, Vol. 2, 73, 1956.
35. D. Langbein, "Non-Retarded Dispersion Energy Between Macroscopic Spheres," *J. Phys. Chem. Solids*, Vol. 32, pp. 1657-1667, 1971.

36. D. Langbein, *Theory of Van der Waals Attraction*, Springer Tracts in Modern Physics, 1974.
37. J.E. Kiefer, V.A. Parsegian, and G.H. Weiss, "Some Convenient Bounds and Approximations for the Many Body Van der Waals Attraction between Two Spheres," *J. Colloid and Interface Science*, Vol. 67, No. 1, pp. 140-153, October 1978.
38. H.W. Marlow, "Survey of Aerosol Interaction Forces," *Aerosol Microphysics I*, W.H. Marlow, editor, pp. 117-156, 1980.
39. N.H. Nayfeh, M.K. Brussel, *Electricity and Magnetism*, 1985.
40. D. McAllister, J.R. Smith, and N.J. Diserens, *Computer Modelling in Electrostatics*, 1985.
41. T. Lozano-Perez, M.T. Mason, R.H. Taylor, "Automatic Synthesis of Fine-Motion Strategies for Robots," *The International Journal of Robotics Research*, Vol. 3, No. 1, pp. 3-24, Spring 1984.
42. M.A. Erdmann. "Using Backprojections for Fine Motion Planning with Uncertainty," *International Journal of Robotics Research*, Vol. 5, No. 1, Spring 1986.
43. B.R. Donald, "A Geometric Approach to Error Detection and Recovery for Robot Motion Planning with Uncertainty," *Artificial Intelligence*, Vol. 37, 1988.
44. J. -C. Latombe, "Motion Planning with Uncertainty: On the Preimage Backchaining Approach," *The Robotics Review I*, O. Khatib, et al, editors, MIT Press, 1989.
45. T. Lozano-Perez, "Spatial Planning: A Configuration Space Approach," *IEEE Transactions on Computers*, Vol. C-32, No. 2, pp. 108-120, February 1983.
46. D. Banks, "Introduction to Microengineering," http://www.ee.surrey.ac.uk/Personal/D.Banks/umintro.html.
47. L.Y. Lin, S. S. Lee, K. S. J. Pister, and M. C. Wu, "Micro-machined Three-Dimensional Micro-Optics for Integrated Free-Space Optical System," *IEEE Photonics Technology Letters*, Vol. 6, No. 12, pp. 1445-1447, December 1994.
48. H. Guckel, "Deep X-ray Lithography for Micromechanics via Synchrotron Radiation," *Nuclear Instruments and Methods in Physics Research B79*, pp. 247-248, 1993.
49. H. Guckel, K.J. Skrobis, T.R. Christenson, J. Klein, S. Han, B. Choi, E.G. Lovel, "Fabrication of Assembled Micromechanical Components via Deep X-Ray Lithography," *Proc. IEEE MEMS '91*, Nara, Japan, pp. 74-79, 1991.
50. T. Tanikawa and T. Arai, "Development of a Micro-Manipulation System Having a Two-Fingered Micro-Hand," *IEEE Transactions on Robotics and Automation*, Vol. 15, No. 1, pp. 152-162, February 1999.
51. Y. Zhou, B.J. Nelson, B. Vikramaditya, "Fusing Force and Vision Feedback for Micromanipulation," *Proceedings of the 1998 IEEE International Conference on Robotics and Automation*, Leuven, Belgium, May 16-20, 1998, pp. 1220-1225.
52. A. Sulzmann, P. Boillat, J. Jacot, "New Developments in 3D Computer Vision for Microassembly," Microrobotics and Micromanipulation, *Proc. of SPIE*, Vol. 3519, pp. 36-47, Boston, November 1998.

53. S. Fatikow and K. Santa, "Planning and Control of a Microassembly Process in a Flexible Microrobot-based Desktop Station," Microrobotics and Micromanipulation, *Proc. of SPIE*, Vol. 3519, pp. 24-35, Boston, November 1998.
54. T. Kasaya, H. Miyazaki, S. Saito, and T. Sato, "Micro Object handling under SEM by Vision-Based Automatic Control," Microrobotics and Micromanipulation, *Proc. of SPIE*, Vol. 3519, pp. 181-191, Boston, November 1998.
55. M. Schuenemann, et. al., "Manufacturing Concepts and Development Trends in the Industrial Production of Microelectromechanical Systems," Microrobots and Microsystem Fabrication, *Proc. of SPIE*, Vol. 3202, Pittsburgh, 1997.
56. M. Schuenemann, et. al., "Modularized Microelectromechanical Devices as Key Components for Advanced Intelligent Autonomous Sensors and Control Systems," Sensors and Controls for Advanced Manufacturing,, *Proc. of SPIE*, Vol. 3201, Pittsburgh, 1997.
57. T.R. Christenson, and D.T. Schmale, "A Batch Wafer Scale LIGA Assembly and Packaging Techniques via Diffusion Bonding," *IEEE MEMS '99*, Orlando, Jan. 17-21, 1999.
58. H. Zhuang and Z.S. Roth, *Camera-Aided Robot Calibration*, CRC Press, Inc. 1996.
59. A. Fox and S. Hutchenson, "Exploiting Visual Constraints in the Synthesis of Uncertainty-Tolerant Motion Plans," *IEEE Transactions on Robotics and Automation*, Vol. 11, No. 1, pp. 56-71, February 1995.

## DISTRIBUTION

| | | | |
|---|---|---|---|
| 1 | MS | 0151 | G. Yonas, 9000 |
| 1 | | 1002 | P.J. Eicker, 9600 |
| 1 | | 1003 | R.D. Robinett, 9611 |
| 1 | | 1008 | J.C. Fahrenholtz, 9621 |
| 1 | | 1010 | M.E. Olson, 9622 |
| 1 | | 1004 | R.W. Harrigan, 9623 |
| 1 | | 1125 | A.K. Miller, 9652 |
| 1 | | 1006 | P. Garcia, 9671 |
| 1 | | 1007 | A.T. Jones, 9672 |
| 1 | | 0329 | D.W. Plummer, 2643 |
| 1 | | 0329 | E.J. Garcia, 2643 |
| 1 | | 0603 | T.E. Zipperion, 1713 |
| | | | |
| 5 | | 0329 | M.A. Polosky, 2643 |
| 10 | | 1003 | J.T. Feddema, 9611 |
| 5 | | 1008 | R.W. Simon, 9621 |
| 5 | | 0329 | T.R. Christenson, 1713 |
| | | | |
| 1 | | 1088 | LDRD Office |
| 1 | | 9018 | Central Technical Files, 8940-2 |
| 2 | | 0899 | Technical Library, 4916 |
| 1 | | 0619 | Review & Approval Desk, 15102 for DOE/OSTI |